Universidade de Aveiro Departamento de Electrónica, Telecomunicações e Informática,
2020

Lucas Sabença Leitão

Sistema de Radar Distribuido Baseado em Fibra Ótica
Photonics-Based Distributed Radar

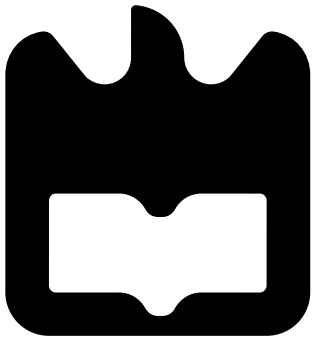

Lucas Sabença Leitão

Sistema de Radar Distribuido Baseado em Fibra Ótica
Photonics-Based Distributed Radar

Dissertação apresentada à Universidade de Aveiro para cumprimento dos requisitos necessários à obtenção do grau de Mestre em Engenharia Eletrónica e Telecomunicações, realizada sob a orientação científica de Paulo Monteiro, Professor do Departamento Eletrónica Telecomunicações e Informática da Universidade de Aveiro e do Doutor Daniel Castanheira, investigador auxiliar no Instituto de Telecomunicações, pólo de Aveiro.

Este trabalho foi desenvolvido no Instituto de Telecomunicações e teve suporte do Fundo Europeu de Desenvolvimento Regional (FEDER), através do Programa Operacional Competitividade e Internacionalização (COMPETE 2020) do Portugal 2020, Projeto RETIOT, POCI-01-0145-FEDER-016432 e da infraestrutura ORCIP, CENTRO-01-0145-FEDER-022141.

o júri / the jury

presidente / president

Professor Doutor Pedro Miguel Ribeiro Lavrador
Professor Auxiliar, Universidade de Aveiro

vogais / examiners committee

Professora Doutora Maria do Carmo Raposo de Medeiros
Professora Associada, Faculdade de Ciências e Tecnologia da Universidade de Coimbra

Professor Doutor Paulo Miguel Nepomuceno Pereira Monteiro
Professor Associado, Universidade de Aveiro

agradecimentos / acknowledgements

Em primeiro lugar, quero agradecer ao meus orientadores, o Professor Paulo Monteiro e o Doutor Daniel Castanheira, por todos os ensinamentos partilhados e apoio prestado, proporcionando as melhores condições para a realização desta dissertação.

Agradeço, também, aos alunos de doutoramento Bruno Brandão e Marco Fernandes, por toda a sua disponibilidade e apoio que sempre demonstraram, bem como ao João Prata, pelo seu profissionalismo.

Aos meus pais, por serem os pilares do meu crescimento pessoal e académico, nunca me faltando com nada. Estou eternamente grato.

À Nicole, a minha parceira de vida, por me apoiar em todo o meu percurso, alinhar em todas as aventuras e por me tornar uma melhor pessoa todos os dias.

À minha irmã, avós, madrinha e tios, por sempre a melhor família que poderia escolher.

Aos meus amigos e colegas de curso do tão queridamente apelidado *Clube dos Mansos*, por todos os nossos momentos de amizade e entreajuda.

À *Ovarense Basquetebol*, por todos os valores transmitidos ao longo do meu percurso enquanto atleta.

A todos os meus professores, colegas e amigos que marcaram o meu percurso até hoje.

Dedico este culminar de 5 anos de trabalho à minha avó Cristiana e ao meu avô Alpoim.

Palavras-chave Radar, Radio-sobre-Fibra, MIMO, OFDM, FMCW, RETIOT

Resumo

A tecnologia Radar tem surgido como uma solução promissora para os novos desafios da sociedade moderna, maioritariamente por ser uma tecnologia flexível e não invasiva, tornando-a assim adequada para uma grande série de aplicações.

Esta dissertação aborda um sistema de Radar distribuído com processamento centralizado e distribuição analógica de rádio-sobre-fibra. Neste contexto, para além de ser feita uma análise a diferentes tipos de onda possíveis de implementar, foi também desenvolvido um simulador que permitiu interpretar a relação que a disposição dos elementos do sistema têm na sua performance. Adicionalmente, foi desenvolvida toda a arquitetura do sistema, que inclui alguns módulos previamente desenvolvidos no âmbito do projeto RETIOT, e outros desenvolvidos testados e analisados na esfera deste trabalho. Por fim, foram feitos alguns testes preliminares ao sistema e uma estimativa do seu comportamento como um todo.

Keywords Radar, Radio-over-Fibre, MIMO, OFDM FMCWRETIOT

Abstract The Radar technology has been presented as a promising solution to the demanding challenges of the modern society, mainly due to its flexibility and non-invasiveness, making it suitable for a wide range of useful applications. This dissertation addresses the development and testing of a distributed Radar system with a central processor and radio-over-fibre signal transport. In this scope, besides analysing different waveforms suitable to be implemented (namely, OFDM and FMCW), a simulator capable of evaluate the relationship between a system configuration/parametrization and its performance was also developed. Additionally, the whole system was engineered, including some modules already developed in the scope of the RETIOT project and others developed, tested and analysed within the scope of this work. Finally, some preliminary testing was made, including the system behavior estimation.

Table of Contents

List of Figures

List of Tables

List of Acronyms

ADAS Advanced Driver-Assistance System. 1

AWG Arbitrary Waveform Generator. 57

AWGN Additive White Gaussian Noise. 7, 13, 14

CWDM Coarse Wavelength Division Multiplexing. 42

DFT Discrete Fourier Transform. 10

E/O Electrical/Optical. 35

EM Electromagnetic. 3

EVM Error Vector Magnitude. 58

FFT Fast Fourier Transform. 10, 12

FMCW Frequency Modulated Continuous Waveform. 8

FODD Foreign-object-debris detection. 1

IC Integrated Circuit. 43

IF Intermediate Frequency. 33

IFFT Inverse Fast Fourier Transform. 12

LO Local Oscillator. 32

MIMO Multiple Input and Multiple Output. 2

MMF Multi-Mode Fiber. 35

MSL Mean Side Lobe. 24

O/E Optical/Electrical. 35

OFDM Orthogonal Frequency Division Multiplexing. 8, 11

OIP3 Third-Order Intercept Point. 43

P1dB 1 dB Compression Point. 43

PAPR Peak-to-Average-Power Ratio. 14

PL Path Loss. 10

PLL Phase-Locked Loop. 32

PSG Vector Signal Generator. 57

PSL Peak Side Lobe. 24

RADAR Radar Detection and Ranging. 1

RadCom Radar-Communication. 21

RCS Radar Cross Section. 2, 10, 55

RF Radio Frequency. 3

RoF Radio Over Fiber. 3

ROSA Receiver Optical Sub-Assembly. 36

RTD Round-Trip Delay Time. 7

SDR Software-Defined Radio. 32, 33

SFP Small Form-factor Pluggable Transceiver. 36

SMF Single-Mode Fiber. 35

SNR Signal to Noise Ratio. 7

SPI Serial Peripheral Interface. 50

TFF Thin-Filmed Filter. 42

TIA Transimpedance Amplifier. 41

TOSA Transmitter Optical Sub-Assembly. 36

USRP Universal Software Radio Peripheral. 33

VGA Variable Gain Amplifier. 43

VNA Vector Network Analyser. 38

VOA Variable Optical Attenuator. 39

VSA Vector Signal Analyzer. 57

WDM Wavelength Division Multiplexing. 42

List of Symbols

$A(X)$ zero Doppler cut of the ambiguity function. 15

B bandwidth. 9

$D_{m,k}$ channel frequency response. 13

K chirp slope. 9

M number of transmitting antennas. 14

M_s number of OFDM symbols. 11

N number of receiving antennas. 14

N_c number of OFDM subcarriers. 11

R range estimation. 7

R_0 target's initial position. 13

T_u chirp period. 9

$X_{m,k}$ digital modulated OFDM data symbol. 12

ΔR range resolution. 10

Δf subcarrier separation. 12

$\hat{X}_{m,k}$ received OFDM symbol. 13

λ wavelength. 7

$\rho_{k,l}(X)$ phase shift as function of X. 16

τ generic delay. 7

$\tau_{k,l}$ time delay of the antenna k/target/antenna l link. 14

$\varphi_{k,l}(X)$ time correlation between the received and transmitted baseband signals for each space point. 15

f_c chirp starting frequency. 9

f_d Doppler shift. 7

$r(t)$ generic received signal. 7

$r^b_{k,l}(t)$ received baseband signal. 14

$r_{k,l}(t)$ received signal after getting reflected by the target. 14, 15

$s(t)$ generic transmitted signal. 7

$s^b_{k,l}(t)$ transmitted baseband signal. 14

v relative velocity estimation. 7

$x(t)$ n-th chirp signal. 9

$x(t)$ OFDM signal. 12

$x_m(n)$ discrete version of the m-th OFDM symbol. 12

$x_m(t)$ mixed FMCW signal. 10

$x_r(t)$ reflected FMCW signal. 9

$y_m(t)$ received OFDM m-th pulse. 13

CHAPTER 1

Introduction

Nowadays, the number of applications in which Radar Detection and Ranging (RADAR) is used is rapidly increasing. From bio sensing, to Advanced Driver-Assistance System (ADAS) and Foreign-object-debris detection (FODD) at the airport runways [1] or even in the context of smart cities, due to its flexibility and non-intrusive nature, Radar based solutions are becoming even more attractive. Following this trend, new distribution and processing techniques of distributed Radar systems are now starting to be studied to overcome the resolution and flexibility problems of stand-alone and local Radar, providing an innovative networked and distributed vision.

1.1 Motivation and context

In the late 19th century, Heinrich Hertz experimentally proved Maxwell's earlier theoretical work on electromagnetism, which led to the conclusion that radio waves are reflected from metallic objects and refracted by a dielectric medium. However, it was not until the middle of the 20th century, during the second world war that systems following these principles started to be widely developed[2]. At this time, Radar technology was of great interest, since it provided an extra degree of precious "vision". This technology provided great advantages in detecting enemies during war, so several nations started developing their own Radar systems to detect stealth targets. Later on, some new features were studied and implemented, being one of them the instantaneous evaluation of a target's velocity, by recurring to the Doppler effect. For a long time, Radar was a military exclusive technology (where target's range, velocity resolutions were low and target's direction were acquired by mechanically rotating antennas) [3].

With the normal technological evolution, new Radar systems with smaller antennas and higher resolutions are now attainable. Also, the increasing demand on high performance Radar systems, triggers the necessity of Radar systems' fusion. Following this trend, Radar systems transitioned from a classical monostatic Radar (which has several limitations in terms of range and cross-range resolution) to new innovative approaches, with several Radar sites and with a wider vision. In this way, multistatic Radar systems appeared. These systems are formed by several independent, stand-alone radars where each one performs local processing and then each of the individual outcomes is sent to a central unit in order to integrate all the

pre-processed data. However, since this scheme assumes a preprocessing, it will inevitably have some information losses.[4]

Multiple Input and Multiple Output (MIMO) systems are defined as systems handling multiple transmitting waveforms and jointly processing signals from multiple receiver antennas [5]. These systems revolutionized the wireless communication systems and their premises are now object of study, so they are extended to MIMO Radar systems.

There are two types of MIMO Radar architectures: collocated and widely distributed. The first one, is based on waveform diversity, whereas in the latter the focus is on the spatial diversity gains. Both approaches achieve an improved localization performance when compared with single Radar sites. Also, for both approaches, it was demonstrated that there is a significant improvement from using a coherent processing approach (there is phase coherence throughout the whole system) [6].

In this context, a centralized MIMO system with widely separated transmitter and receiver antennas is able to exploit its spatially distributed information to generate richer backscatters [5], and consequently, improving the target detection/localization performance, specially when considering complex targets (by taking advantage of their spatial diversity, or when its Radar Cross Section (RCS) is low)[7],[8]. Thus, it is of great interest to study these widely separated MIMO systems due to their wide applicable scenarios: From detecting object debris in an airplane runway, to get more precise and accurate ADAS systems or even to be implemented in future smart systems. With this high performance and being Radar technology a non-invasive vision system, the use case possibilities are endless. However, MIMO radars with widely separated antennas have some constraints that prevent these systems to be already deployed: they need high capacity/low loss data links for the communication between the antennas and the central processor; and they require precise time and phase synchronization in order to perform the coherent processing, which is vital to achieve its high resolution. Since RF-based systems are not able to attain these requirements, photonics-based Radar systems are captivating attentions due to their frequency flexibility and phase noise stability [9][10]. Photonics also enables the implementation of a distributed coherent Radar network by allowing the signal generation in a single central unit and consequently distribution to remote Radar sites [11].

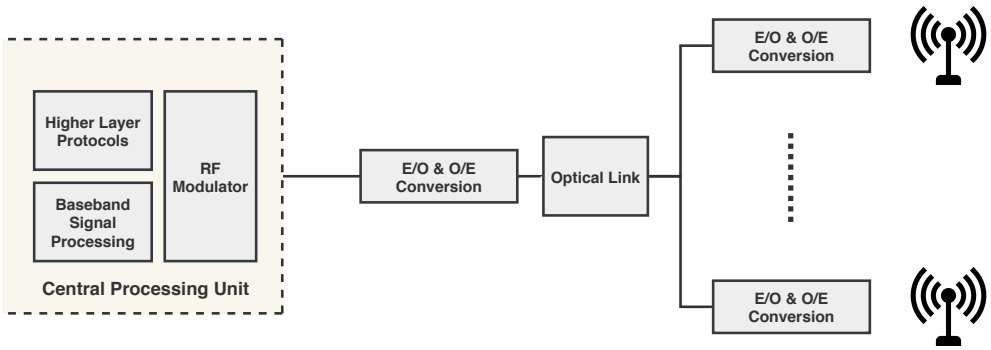

Figure 1.1: *Radio over Fiber* example scheme

Given this background, Radio Over Fiber (RoF) technology (in which a light signal is modulated by a radio signal and then transmitted over an optical fiber link) allows the low loss Radar signals distribution over greater distances (from a central unit to a remote Radar side) without Electromagnetic (EM) interferences. [12]. Also, considering a generic RoF architecture as depicted in figure 1.1, by moving the higher layer and signal processing functions to a unique central unit, the system's architecture gets simplified, becoming transparent to modulation and signal formatting, as well as being prone to upgrades and maintenance simplification. Thus, with the maturation of microwave photonics, a widely distributed Radar system with a central MIMO coherent processing unit is achievable, as the first coherent photonics-based Radar system [9] and some recent investigations tested in a real outdoor scenario with multiple closely-spaced targets [6] proven.

1.2 Objectives

The main focus of this dissertation is to study and implement a photonics-enabled widely distributed RADAR system with MIMO processing. In this way, the work objectives can be divided into a simulation part and an hardware implementation part:

- Simulation Part
  - Study and simulation of different MIMO processing algorithms, regarding two different waveforms and with the goal of achieving a better range/cross-range resolution.
  - Other factors such as the number of antennas and their positioning are also investigated, in order to attain the best possible results with the available hardware
- Hardware Implementation Part
  - Design and implementation of a Radio Over Fiber (RoF) transmission link to transport Radar waveforms from/to remote sites/central processing unit.
  - Design, production and characterization of an RF amplifier board.
  - Finally, the goal is to fuse these components with a Radio Frequency (RF) system (in house developed, by the RF group) and perform some preliminary experimental testing to the system.

1.3 Dissertation Outline

In order to attain the objectives stated above, this dissertation has the following structure:

- Radar fundamentals and some waveforms are addressed in chapter 2, in order to get the basic principles of the Radar technology. Also, the *Widely Distributed MIMO Radar* solution is presented and compared with the classic monostatic approach.
- Chapter 3 first defines how the system simulation is build up and what are its main properties. Then, several simulation configurations are described and analysed in order to achieve the best configuration to be used in the experimental setup.

- In Chapter 4, the experimental setup is presented, its components are described and characterized. The component integration is also analysed and some preliminary testing and estimations are made.
- Finally, in chapter 5 conclusions are made, by facing the objectives with the achieved work outputs. Also, possible future work is described.

1.4 Contributions

The work developed within the scope of this dissertation was integrated in the development of the project RETIOT demonstrator. As such, this work was aligned with previous developments made within the RETIOT project context. In the following, the main contributions of this dissertation can be summarized as follows:

1. Study and development of an optical link to be integrated into a reflectometry system integrated in the RETIOT project.
2. Development of a simulator to evaluate the relationship between the configuration/parametrization of a *Widely Distributed Radar System* and its performance.
3. Engineering and characterization of the reflectometry system as a whole.
4. Development and characterization of RF amplifier boards to be integrated in the system.
5. Study of the performance of the developed system in a specific application scenario.
6. Experimentally Testing of a prelminary version of the system.

CHAPTER 2

Radar Principles

A Radar system is an EM system which is able to detect and locate objects. Both detection and ranging have been the core functionality of this kind of systems, however, modern Radars are able to find other types of characteristics of a given target, such as its velocity and cross-range (angle relative to the Radar site). These features are of great interest for several applications (see chapter 1). Also, there are different radio signals that can be incorporated into a Radar system, each one of them with its own unique characteristics.

Firstly, this chapter presents an overview of the Radar fundamentals. Then, two main waveforms are described, explaining how they can be exploited to obtain a workable monostatic Radar system. Finally, the *Widely Distributed MIMO* approach is presented and compared with the monostatic vision.

2.1 Radar Fundamentals

A Radar system can be categorized as a monostatic or multistatic system. In a monostatic system, both the transmitter and receiver are located in the same place. A multistatic system can have several transmitters and several receivers in different space positions. In this case, each receiver can process the information independently of the other receivers or all the received information can be jointly processed. These multistatic systems are discussed in detail in chapter 2.3.

In a monostatic Radar system, a Radar EM waveform is transmitted over the air, then it is intercepted/reflected by a target and part of the reflected waveform is received by the Radar system (see figure 2.1). Afterwards, the information received is processed to obtain the target's characteristics, such as range and velocity.

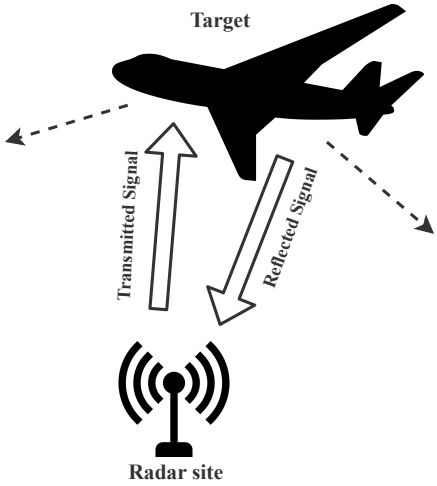

Figure 2.1: *Monostatic Radar* scenario

A generic Radar system can be described by the diagram depicted in figure 2.2. The Radar signal is generated at a low power level and then it is modulated to the desired Radar frequency (the Radar waveform is generated at low power in order to be flexible in terms of generation of different signals). After that, the waveform is amplified through a power amplifier. The duplexer enables the same antenna to transmit and receive signals (it protects the receiver from the leakage of the high power signal of the transmitting signal path). When the duplexer connects the antenna to the receiver circuitry, it allows the reflected signal to pass through a low noise amplifier (to minimize the impact in the noise figure) and then by a mixer, which mixes the received signal with a local oscillator and whose output is the intermediate frequency signal. The signal then passes through a matched filter(see section 2.1.1), whose output is used to get the target's characteristics.

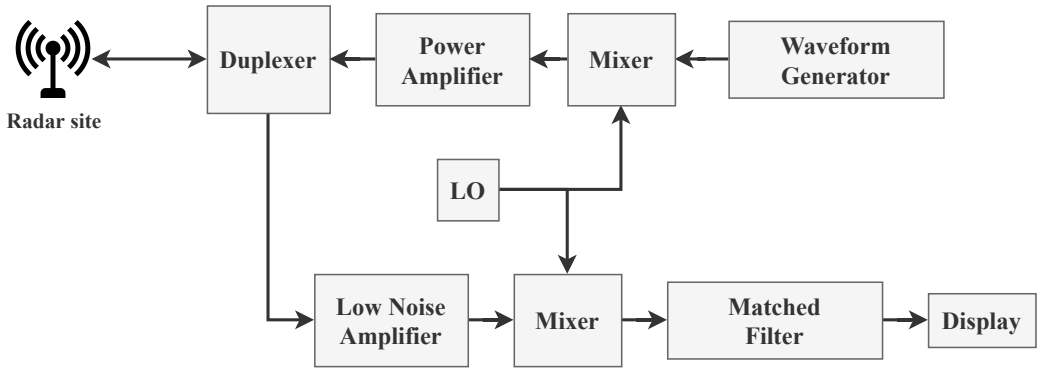

Figure 2.2: Block diagram of a generic Radar system

2.1.1 Matched Filter

The processing block represented in the block diagram of figure 2.2 is of great importance. The matched filter maximizes the Signal to Noise Ratio (SNR) of a given received signal in the presence of noise and its output corresponds to the correlation of the received signal with the template one. Considering a Radar system, by correlating the reflected signal with the transmitted one (template), it is possible to get the time delay for which the reflected signal approximates the most to the known transmitted waveform. The detection expression is the following [13]:

$$\begin{aligned} Y(\tau, f_d) &= \int (r(t) + n(t)) s(t-\tau)^* e^{-j2\pi f_d t} dt \\ &= \int r(t) s(t-\tau)^* e^{-j2\pi f_d t} dt + \int n(t) s(t-\tau)^* e^{-j2\pi f_d t} dt \end{aligned} \tag{2.1}$$

where $r(t)$ is the reflected signal, $s(t-\tau)$ is a delayed version of the transmitted signal ($s(t)$) and $n(t)$ is Additive White Gaussian Noise (AWGN). The f_d represented in the exponential term is a Doppler frequency shift that is proportional to the target's velocity (details in 2.1.3). The noiseless term of expression 2.1 represents the template/received signal mismatch whereas the second term represents how the noise affects the output. In order to accurately estimate the received signal delay, the detection threshold value must be chosen so a good trade-off between quality of detection and false positives is achieved.

2.1.2 Range

A target's range is the 1D distance between the Radar system and the target. In order to estimate the range, time synchronization is required. Following the matched filter expression (2.1), the (τ) variable is the delay for which the correlation between the transmitted/reflected signals is maximum. So, by applying the simple time/velocity/distance relation, we can express the target's range (R) as:

$$R = \frac{\tau c_0}{2} \tag{2.2}$$

being c_0 the propagation velocity of an EM waveform, which is approximately equal to the speed of light ($c_0 = 3 \times 10^8 m/s$) and the 1/2 factor being related to the Round-Trip Delay Time (RTD) path.

2.1.3 Velocity

To estimate the velocity of a target, Radar systems rely on the known Doppler effect. This effect establishes a relation between an object's velocity and the frequency shift (Doppler shift) it produces when hit by an EM waveform. The Doppler expression is the following:

$$f_D = \frac{2v}{\lambda} \tag{2.3}$$

where v represents the velocity of the object in relation to the Radar system and λ is the wavelength. Thus, the Doppler shift value may be positive or negative, if the object is moving closer or further away, respectively. In this case, the delay (τ) caused by a target is given by[14]:

$$\tau = \frac{2(R_0 \pm vt)}{c_0} \tag{2.4}$$

where R_0 is the target's initial position. Along these lines, a great way to determine the velocity of a target is to perform the same correlation operations described in the matched filter (see expression 2.1) but this time as a function of Doppler frequency f_d (see 2.3). By doing this, it is possible to obtain the frequency which maximizes the SNR, thus, getting the correspondent Doppler shift and through 2.4, the target's velocity.

2.1.4 Direction

In a scenario with several targets, whose range/velocity are not resolvable (as depicted in 2.3), the direction of the target in relation to the antenna system might solve the problem.

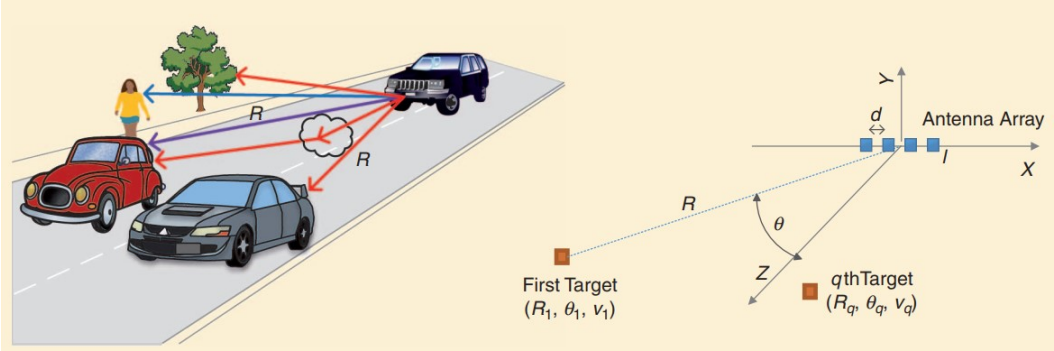

Figure 2.3: Scenario with multiple targets (left) and representation of an antenna array Radar system (right)[14].

In order to estimate the direction of a target, an antenna array must be considered. To perform this estimation, a spherical coordinate system (R, θ, ϕ) is used, where the (θ, ϕ) are the azimuth/elevation angles. Considering a target with position (R, θ) moving with velocity v, the RTD time between a transmitter at the origin and a receiver distanced l in the same axis is given by [14]:

$$t_d = \frac{2(R_0 \pm vt) + ldsin\theta}{c_0} \tag{2.5}$$

where d is the spacing between antenna elements. With this antenna array system, the delay term (t_d) creates a uniform phase progression across the antenna elements, enabling the estimation of the angle by correlating signals in the spatial domain.

2.2 Radar Waveforms

There is a great variety of waveforms suitable for Radar systems, thus this waveform diversity is converted into a variation in some Radar performance metrics, such as range/velocity range and resolution, SNR and probability of target detection. According to the characteristics of the system to study in this dissertation, two main waveforms were chosen to be studied: Frequency Modulated Continuous Waveform (FMCW) and Orthogonal Frequency Division Multiplexing (OFDM)

2.2.1 FMCW Waveform

From the several waveforms suitable for Radar applications, FMCW presents unique features that enable the joint range/velocity target detection, with a good SNR and with a sweep duration independently of the bandwidth. The FMCW waveform is characterized by having a repetition of chirps over time. As depicted in 2.4, one possible example of a chirp is a sine wave whose frequency increases linearly with time:

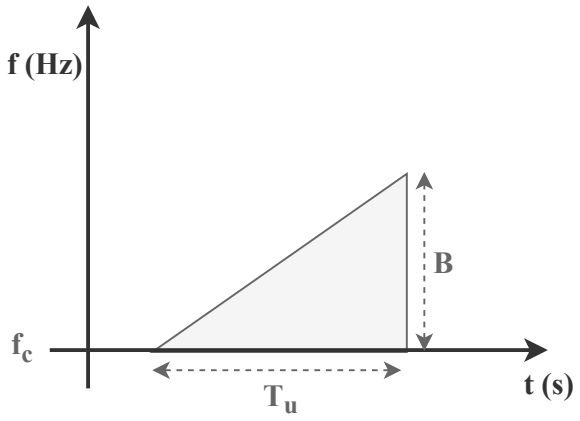

Figure 2.4: Chirp signal

The mathematical representation of the chirp signal is given by [15]:

$$chirp(t) = e^{j2\pi(f_c t + \frac{Kt^2}{2})} \tag{2.6}$$

where B is the signal bandwidth, T_u is the chirp period and f_c is the starting frequency.

The chirp slope (K) is given by:

$$K = \frac{B}{T_u} \tag{2.7}$$

Expression 2.6 only describes one chirp. In order to describe the FMCW signal as a whole, the n-th chirp must be distinguishable, so we can consider t_s as the time from the start of the n-th chirp[15]:

$$t = nT_u + t_s \quad where \quad 0 < t_s < T_u \tag{2.8}$$

Therefore, the n-th chirp signal signal is given by:

$$c(t) = e^{j2\pi(f_c(nT_u + t_s) + \frac{Kt_s^2}{2})} \tag{2.9}$$

Range estimation

Considering a static target, the reflected FMCW signal will be [16]:

$$c_r(t) = \alpha e^{j2\pi(f_c(nT_u + t_s - \tau) + \frac{K(t_s-\tau)^2\tau}{2})} \tag{2.10}$$

Where α is a complex scalar, which represents the antenna gains, the target's Radar Cross Section (RCS) and the Path Loss (PL). The RTD of the transmitted signal is represented by τ, and is related to the target's range (R):

$$\tau = \frac{2R}{c_0} \tag{2.11}$$

The received signal must then be mixed with the transmitted signal [16]:

$$c_m(t) = c(t)^* \times c_r(t) \tag{2.12}$$

After some simplifications, the mixed FMCW signal is given by [16]:

$$c_m(t) = \alpha e^{j2\pi(f_c\tau + Kt\tau - \frac{K}{2}\tau^2)} \tag{2.13}$$

By substituting τ with its equivalent in (2.11):

$$c_m(t) = \alpha e^{j2\pi(\frac{2f_cR}{c_0} + \frac{2KR}{c_0}nT_u + \frac{2KR}{c_0}t_s - \frac{2KR^2}{c_0})} \tag{2.14}$$

where the third term denotes the beat frequency (f_b) and is related to how the signal changes over one chirp time:

$$f_b = \frac{2KR}{c_0} \Leftrightarrow R = \frac{f_b c_0}{2K} \tag{2.15}$$

So, by doing the Fast Fourier Transform (FFT) (efficient algorithm which applies Discrete Fourier Transform (DFT)) of the signal over one chirp time, the peak of the obtained frequency response corresponds to f_b, from which we may estimate the target range:

$$R = \frac{f_b c_0}{2K} \tag{2.16}$$

The minimum distance where two targets are distinguishable, i.e. the range resolution, is based on the fact that the frequency resolution of the mixed signal is lower bounded by the chirp frequency ($\Delta f_b \geq \frac{1}{T_u}$). Substituting K with equation 2.7, the range resolution can be obtained:

$$\Delta f_b = \frac{2B\Delta R}{c_0 T_u} \Leftrightarrow \Delta R = \frac{c_0}{2B} \tag{2.17}$$

Velocity estimation

To get a target velocity estimation, the Doppler effect is used. According to this phenomena, when a target is moving with a certain velocity v, the reflected EM wave will suffer a frequency shift proportional to the relation of the target/emitter relative velocities (see section 2.1.3). Since the target is moving, the received waveform delay τ expression also has a velocity component:

$$\tau = \frac{2(R + vt)}{c_0} \tag{2.18}$$

Replacing τ (with its new equivalent) in (2.13), and after doing some simplifications [16], the new $c_m(t)$ expression is approximated as:

$$c_m(t) = \alpha e^{j2\pi(\frac{2KR}{c_0}t_s + \frac{2f_cv}{c_0}nT_u + \frac{2f_cR}{c_0})} \tag{2.19}$$

By analysing this equation, it is possible to check the relation of the frequency and the target's range in the first exponential term. The third one is a constant phase term. The second term is a phase which is associated with f_b and is an indication of the signal changes along the number of chirps (Doppler shift).

To find the Doppler shift, a second FFT (having as input the output of the FFT over one chirp period) can be performed over the consecutive chirp periods. Thus:

$$f_d = \frac{2f_c v}{c_0} \Leftrightarrow v = \frac{f_d c}{2f_c} \tag{2.20}$$

This 2D joint processing algorithm of first applying the FFT over the chirp time and then apply another FFT over the output of the first one, provides a range-Doppler map as, figure 2.5 depicts:

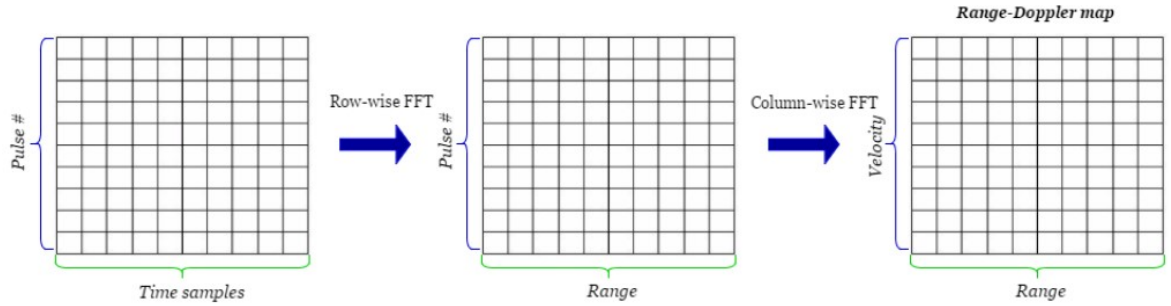

Figure 2.5: 2D FFT processing summarized [16]

2.2.2 OFDM Waveform

The Orthogonal Frequency Division Multiplexing (OFDM) signal is commonly known from its communications functions, but by integrating it into a Radar system, it enables to jointly detect targets and communicate with them. By doing so, OFDM empowers new use cases following new technology trends [17].

In an OFDM system, a high-rate continuous datastream is split into lower rate parallel streams. Each one of these M_s parallel streams is transmitted over N_c different subcarriers, being the subcarriers uniformly spaced in the frequency domain, thus granting orthogonality between them.

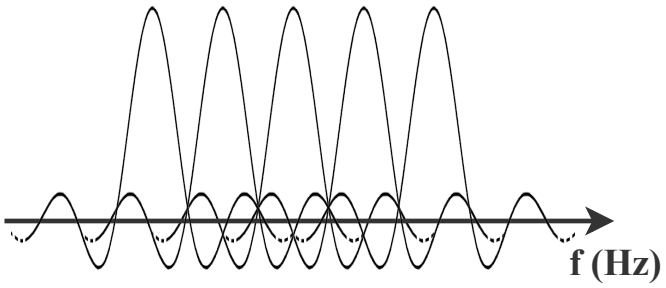

Figure 2.6: OFDM signal representation in the frequency domain

To generate all the subcarriers, several shaping filters were needed, making it impractical with numerous subcarriers. Due to the OFDM signal properties, these filters are no longer needed, since the same operations can be made using the IFFT/FFT algorithms.

We can express the OFDM signal, as a sum of data symbols times their correspondent subcarriers, thus, the output of the IFFT (OFDM time domain transmitted signal) is the sum of N_c orthogonal sinusoids:

$$x(t) = \sum_{m=0}^{M_s-1} \sum_{k=0}^{N_c-1} X_{m,k} e^{j2\pi k\Delta f t} rect(t, m) \tag{2.21}$$

where $X_{m,k}$ represents a digital modulated data symbol (PSK or QAM symbol, for example), and the exponential part corresponds to the k-th subcarrier. The $k\Delta f$ term guarantees that all the subcarriers are orthogonal to each other (as depicted in 2.6) and $rect(t, m)$ is given by:

$$rect(t, m) = \begin{cases} 1, & mT \leq t < mT + T \\ 0, & otherwise \end{cases} \tag{2.22}$$

So, the expression in 2.21, represents an OFDM signal with M_s symbols with a duration of T each. All OFDM symbols have N_c subcarriers with a separation of Δf. The schematic in figure 2.7 is a representation of the OFDM signal:

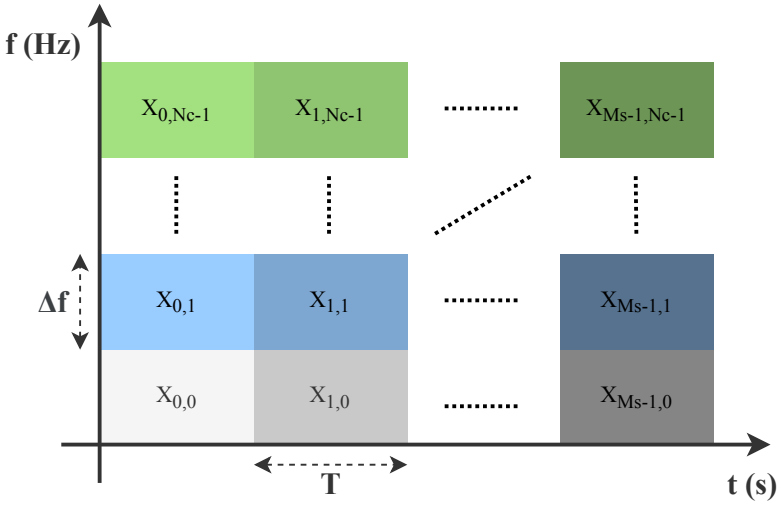

Figure 2.7: OFDM signal schematic

Considering the m_{th} symbol, to perform its IFFT, we must consider an IFFT length of N_c and replace the time variable by the sampling period (which must be at least 2 times the maximum frequency of the signal, according to the Nyquist law):

$$t = nT_s = \frac{n}{N_c \Delta f} \tag{2.23}$$

By substituting t in 2.21 for its correspondent in 2.23, the following discrete version of

the m-th OFDM symbol is given:

$$x_m(n) = \sum_{k=0}^{N_c-1} X_{m,k} e^{j2\pi k \frac{n}{N_c}} \tag{2.24}$$

This expression represents the inverse transform used in the FFT algorithm. Thus, each OFDM symbol is transmitted over N_c time samples with a duration of $T = \frac{N_c}{B}$.

The original modulated data, can be recovered by sampling the signal in 2.24 at a rate of N_c/T and performing the FFT over the N samples, afterwards.

Range Estimation

Considering a static target at a distance R, the received OFDM m-th pulse, in the time domain is:

$$y_m(t) = \sum_{k=0}^{N_c-1} X_{m,k} e^{j2\pi k \Delta f (t-t_d)} + \eta(t) \tag{2.25}$$

being t_d the RTD and $\eta(t)$ the AWGN and:

$$y_m(t) = \sum_{k=0}^{N_c-1} X_{m,k} e^{j2\pi k \Delta f (t-t_d)} + \eta(t) \tag{2.26}$$

Discarding the noise, the received OFDM symbol is given by:

$$\hat{X}_{m,k} = X_{m,k} e^{j2\pi k \Delta f (-t_d)} \tag{2.27}$$

We can conclude that the distortions caused by the channel are contained in the received OFDM symbol $\hat{X}_m(t)$. Thus, by comparing the transmitted and received symbols, we get:

$$D_{m,k} = \frac{\hat{X}_{m,k}}{X_{m,k}} \Leftrightarrow D_{m,k} = e^{j2\pi k \Delta f (-t_d)} \tag{2.28}$$

where $D_{m,k}$ is the channel frequency response. The impulse response of the channel containing the range profile of the target can be obtained by doing an IFFT:

$$z(k) = IFFT[D_m], k = 0, 1.., N_c - 1 \tag{2.29}$$

Velocity Estimation

When considering a moving target, the signal will also have a Doppler shift relative to the target's velocity. In this case, we can define:

$$R = R_0 + v(t + mT) \tag{2.30}$$

where R_0 is the target's initial position and mT represents the delay associated with the m-th symbol (T is the duration of each symbol). Considering that the signal bandwidth $B \ll f_c$, we can assume that each subcarrier has the same Doppler shift f_d. Also, $f_d \ll f_c$ therefore, the received OFDM signal expression in 2.27 can be rewritten as:

$$\hat{X}_{m,k} = X_{m,k} e^{j2\pi f_D mT} e^{j2\pi k \Delta f (-t_d)} \tag{2.31}$$

In this way, the expression 2.28 can also be rewritten to include the Doppler effect:

$$D_{m,k} = e^{j2\pi f_D mT} e^{j2\pi k\Delta f(-t_d)} \tag{2.32}$$

Since it is assumed that Doppler affects equally all the subcarriers, a target's velocity can be estimated by performing the FFT through the time axis of the channel transfer function (obtaining an estimate of the Doppler term):

$$z(m) = FFT[D_k], m = 0, 1.., M_s - 1 \tag{2.33}$$

As an alternative, both velocity/range can be estimated by first performing the FFT over the time axis and then performing the IFFT over the frequency axis (over each OFDM symbol):

$$Z(k, m) = IFFT[FFT[D]] \tag{2.34}$$

Also, one important characteristic of the OFDM signal must be taken into account for the future setup integration: its high Peak-to-Average-Power Ratio (PAPR) (due to having several subcarriers adding up). This factor, that is important for signal saturation issues, for an OFDM signal with 8 subcarriers and QPSK modulation (which is the case, as detailed in section 3) represents a maximum power fluctuation value of $10log(8) = 9dB$, approximately [18]. However, there are several PAPR reduction techniques that can be used to mitigate this [19].

2.3 MIMO Radar with Widely Distributed Antennas

In the previous sections, monostatic Radar approaches are considered, where their range resolution is limited by the bandwidth of the signal and the cross-range resolution depends on the antennas beam aperture. The novel approach described in this section, is a breakthrough in the traditional stand-alone Radar, presenting a new distributed vision. Also, it is given the first insight in how this solution can be implemented in a real setup.

2.3.1 Signal Model

To interpret this new approach, we should consider M transmitting antennas and N receiving antennas. The M transmitted signals are assumed orthogonal (orthogonality can be achieved by time, frequency or space multiplexing). Now, considering a single target at coordinates $X = (x, y)$ in a 2D Cartesian's plane and a transmitting antenna (k) and a receiving one (l), the model of the received signal after getting reflected by the target is represented by [13]:

$$r_{k,l}(t) = \alpha s_k(t - \tau_{k,l}(X)) + n_{k,l}(t) \tag{2.35}$$

The signals in 2.35 are of the form $r_{k,l}(t) = r^b_{k,l}(t)e^{j2\pi f_c t}$ and $s_{k,l}(t) = s^b_{k,l}(t)e^{j2\pi f_c t}$, where $r^b_{k,l}(t)$ and $s^b_{k,l}(t)$ are the baseband received/transmitted signals, respectively, and the exponential term represents the phase shifts due to the carrier frequency, f_c. The factor α depends on the target's RCS, the antenna gain, the PL and the carrier frequency and $\tau_{k,l}$ is the time delay, given the distance between the target and both the transmitter/receiver antennas. The noise is represented as $n_{k,l}$ and is modelled as AWGN. One important thing to take notice

is that when considering the non-coherent method only the baseband signals are considered, whereas in the coherent case, the carrier information must be taken into account.

Assuming orthogonality between transmitted waveforms, the receiver antennas can separate each one of the signals. Thus, the received signals may be represented by a $MN \times 1$ vector:

$$R(t) = [r_{1,1}(t), ..., r_{M,N}(t)]^T \tag{2.36}$$

2.3.2 Processing Algorithms

After getting all the $M \times N$ received signals (see 2.36) a joint processing is made. The processing algorithms follow a log-likelihood function (described in detail in [13]) so the correlation between the received signal and a delayed version of the transmitted signal is made for each possible location ($X = (x, y)$) [13]:

$$\begin{aligned} L_X(r(t)|X) &\propto \left| \sum_{l=1}^{N} \sum_{k=1}^{M} \int r_{k,l}^*(t) s_{k,l}(t - \tau_{k,l}(X)) dt \right|^2 \\ &\propto \left| \sum_{l=1}^{N} \sum_{k=1}^{M} e^{-j2\pi f_c(\tau_{k,l}(X))} \int {r_{k,l}^b}^*(t) s_{k,l}^b(t - \tau_{k,l}(X)) dt \right|^2 \end{aligned} \tag{2.37}$$

where $r_{k,l}(t)$ is the received signal after getting reflected by a target (as modeled in 2.3.1), $s_{k,l}(t, X)$ is the transmitted signal delayed as a function of X and the exponential term represents the phase shifts due to the carrier frequency as function of X. As explained in the previous section, for the non-coherent method, the carrier information is not considered, so the exponential term in expression 2.37 must be ignored. However, for the coherent method, the carrier information takes an important role in target detection. Thus, these two methods present major differences regarding their performance.

To compare both methods' performance, a unique target is assumed to be centered at origin ($\tau_{k,l}(X_0) = 0$). Then we could define the function $A(X)$ as the zero Doppler cut of the ambiguity function. This zero Doppler cut of the ambiguity function is nothing more than the output of a matched filter. In this way, we can check the existent ambiguities, thus obtaining the range/cross-range resolution of each method.

Non-Coherent Processing

For the non-coherent processing, the ambiguity function is defined as it follows [5]:

$$A(X) = \frac{1}{MN} \left| \sum_{l=1}^{N} \sum_{k=1}^{M} \varphi_{k,l}(X)) \right|^2 \tag{2.38}$$

where $\varphi_{k,l}(X)$ represents the time correlation between the received and transmitted baseband signals for each processing window's point:

$$\varphi_{k,l}(X) = \int r_{k,l}^b(t) {s_{k,l}^b}^*(t - \tau_{k,l}(X)) dt \tag{2.39}$$

This ambiguity function is translated into the following resolution [11]:

$$\Delta R_{non-coherent} \approx \frac{c_0}{2B} \tag{2.40}$$

being c_0 the speed of light. The expression above represents an inverse proportional relation between the Radar's range/cross-range resolution and the signal bandwidth (B).

Coherent Processing

Considering now a coherent processing, the ambiguity function is given by [5]:

$$A(X) = \frac{1}{MN} \left| \sum_{l=1}^{N} \sum_{k=1}^{M} \rho_{k,l}^{*}(X) \varphi_{k,l}(X)) \right|^2 \tag{2.41}$$

which represents a time/space correlation, where $\rho_{k,l}(X)$ is the phase shift as function of X:

$$\rho_{k,l}^{*}(X) = e^{-j2\pi f_c(\tau_{k,l}(X))} \tag{2.42}$$

This is translated into a range/cross-range resolution expressed as it follows [11]:

$$\Delta R_{coherent} \approx \frac{c_0}{f_c} \tag{2.43}$$

In this coherent approach, the range/cross-range resolution is of the order of the carrier wavelength (depends only on the carrier frequency (f_c)). Thus, we can achieve better resolutions by using carriers with several GHz, without being limited by the signal bandwidth.

2.3.3 Comparison Between Monostatic and Widely Distributed Radar

The *Widely Separated MIMO* model described in this section has several advantages over the simple monostatic solutions presented in the previous sections. First, thanks to this distributed vision, it is possible to generate a 2D mapping of the space, as opposed to the 1D range only capability of the simple monostatic systems. Another important point is that with this model, by exploiting a target's RCS diversity, an improved Radar performance can be achieved. It is indisputable that this flexibility opens up different implementation advantages, being the major advantage, the one when considering a coherent approach. Since the coherent resolution only depends on the carrier frequency (see 2.43), the signal bandwidth constraints disappear, empowering new systems with a much better resolution, regardless of the waveform bandwidth.

However, this model also presents some limitations, especially when considering the coherent approach. In this case there must be a precise time and phase synchronization between all the components of the system. Also, it assumes that there is no multipath propagation and no direct links between transmitting and receiving antennas. Both of this unconsidered effects may cause interferences in the receiving signal's amplitude and phase.

CHAPTER 3

System Simulation

Here, a MATLAB simulator based on a MIMO system is presented. This system enables two possible processing approaches, and each approach is described and analysed in this chapter. Also, the whole simulation procedure is interpreted and its results are investigated in order to achieve the best compromise between performance and some hardware requirements. In appendix A, the simulator code is presented (for the configuration with the best results).

3.1 Simulation Model and its Attributes

Firstly, the signal model described in section 2.3 is considered for the simulation, where both the antennas and targets are considered as isotropic dots with unitary gain (i.e. the antennas are considered to transmit in all directions and targets also reflect in all directions). Furthermore, targets also introduce a unitary phase shift to the signals they receive and regarding the received signal, they do not contemplate secondary reflections(i.e. for each pair of antennas, only the antenna-target-antenna path is modeled).

Following those parameters and considering one target, the expression 2.35 of the signal at the l-th receiver is modeled by:

$$r_{k,l}(t) = s_k(t - \tau_{k,l}(X_{target})) + n_{k,l}(t) \tag{3.1}$$

For the non-coherent approach, after getting all the received signals, the correlation of each received signal ($r_{k,l}$) with a delayed version of $s_{k,l}$ (discarding the carrier information) for each possible position of the radar space $X = (x, y)$ is performed, following expression 2.37. So, for each pair of transmitter/receiver antennas, an iso-range curve is generated (i.e. the curve which represents the points in the 2D space where the delay from transmitter-point(X)-receiver is the same). By jointly processing these outputs, the result is the radar space heat map.

Turning now to the coherent analysis, besides the algorithm being the same for both non-coherent and coherent approaches, the latter takes into account the carrier information, instead of only correlating the baseband signals.

The radar image is divided in $128_{px} \times 128_{px}$ pixels, each one corresponding to a possible target position. The likelihood function must be computed for each image pixel.

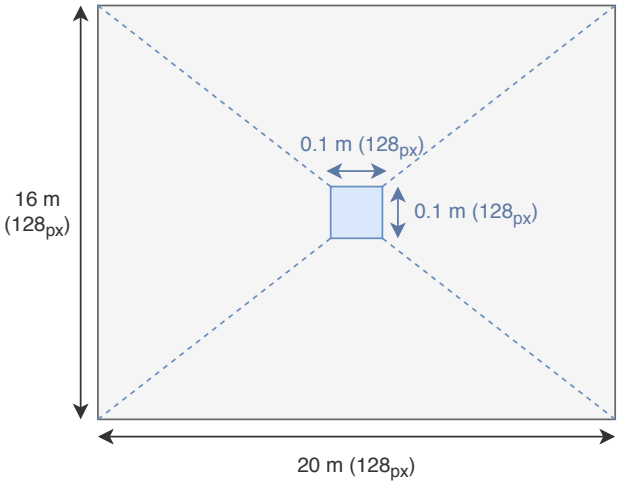

Figure 3.1: Radar processing space (non-coherent in grey, coherent in blue)

As depicted in 3.1, the radar space that is considered for the coherent processing is just a fraction of the space for the non-coherent approach. This choice was made in order to set a compromise between radar resolution and computational effort.

Due to its great performance and flexibility, the widely separated MIMO model described in section 2.3 is the one to be integrated in the RETIOT demonstration setup, which had some hardware requirements defined *a priori* that influenced important parameters to take into account for simulation:

Parameters	**Value**
B	100 MHz
f_c	28 GHz
N_r Transmitter	4
N_r Receivers	4

Table 3.1: Setup main parameters

The parameters expressed in table 3.1 are the key ones for the system (description of the whole experimental setup can be found on chapter 4), so by substituting in 2.40 and in 2.43:

$$\Delta R_{non-coherent} = \frac{c_0}{2 \times 100e6} = 1.5m \tag{3.2}$$

$$\Delta R_{coherent} = \frac{c_0}{28e9} = 0.01m \tag{3.3}$$

we can have a perception of the resolutions we should expect for this system. The expressions in 3.2 and 3.3 also justify the radar processing space choices for the radar space (depicted in figure 3.1).

In sum, this simulator enables the testing of several antennas/targets dispositions, so the best disposition for the setup is chosen. It is also flexible in terms of the waveforms it supports, so we can do simulations for both FMCW and OFDM signals. Taking into account all of these presets, this simulator makes possible to analyse not only how the disposition of the antennas affect the radar performance, but also to check the gains that a coherent system produces, in relation to the simpler non-coherent system.

3.2 Simulation Results

From expressions 3.2 and 3.3 we see that only the bandwidth of the signal and carrier frequency (respectively) are relevant in terms of resolution, so either FMCW and OFDM baseband signals will produce the same output if the parameters are similar. To prove so, first we should consider the two waveforms (FMCW and OFDM) with the same bandwidth and the same carrier frequency (according to the setup parameters, 4.9):

Chirp Parameters	**Value**
B	100 MHz
T_u	150 μs
$N_{samples}$	128
f_c	28 GHz

Table 3.2: FMCW parameters

OFDM Parameters	**Value**
B	100 MHz
$QPSK_{nr.symbols}$	8
$N_{subcarriers}$	8
f_c	28 GHz

Table 3.3: OFDM parameters

Now, considering a target at the origin and a random deployment of 8x8 transmitting/receiving antennas:

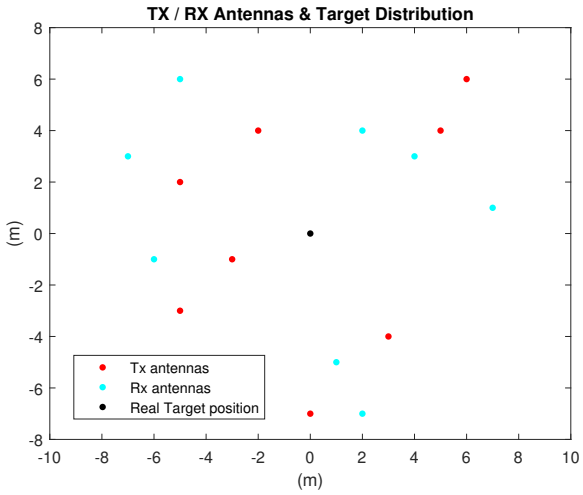

Figure 3.2: Antennas and targets distribution

both the non-coherent/coherent methods are tested for the two waveforms, whose results are depicted in figures 3.3 and 3.4:

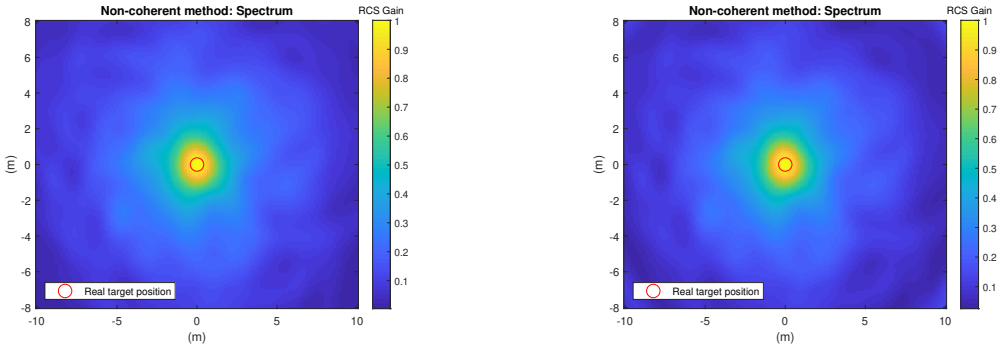

(a) OFDM waveform (b) FMCW waveform

Figure 3.3: Non-coherent processing: OFDM and FMCW comparison

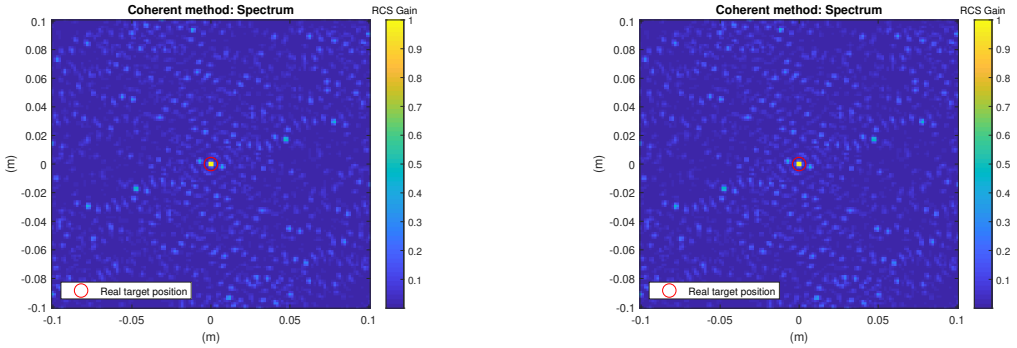

(a) OFDM waveform (b) FMCW waveform

Figure 3.4: Coherent processing: OFDM and FMCW comparison

As we can see, the results are the same regardless of the waveform. Therefore, by taking into account the great potential of the OFDM waveform integration in future Radar-Communication (RadCom) systems (as explored in [17]), from now on, all the presented configurations and their results evaluation will be regarding the OFDM waveform.

In the next subsections different configurations will be analysed and compared.

3.2.1 Configuration 1 - Random Distribution of 4Tx/4Rx Antennas with 2 Distant Targets

In this first configuration, a random space deployment of 4 transmitting antennas and 4 receiving antennas with two separated targets is simulated:

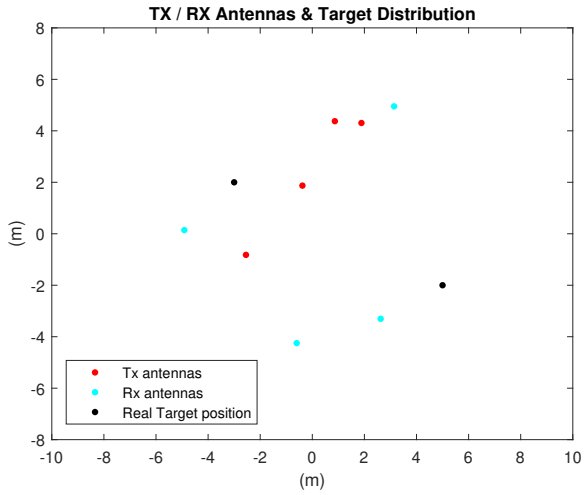

Figure 3.5: Configuration 1 - antennas and targets distribution

The black dots, correspond to two targets, whose distance is higher than the non-coherent radar resolution (1.5 meters). The targets coordinates are expressed in table 3.4:

Targets	**Position (x,y) (m)**
Target 1	(-3,3)
Target 2	(5,-2)

Table 3.4: Targets positions

Non-Coherent Processing

By performing the non-coherent method, the following heat map is obtained:

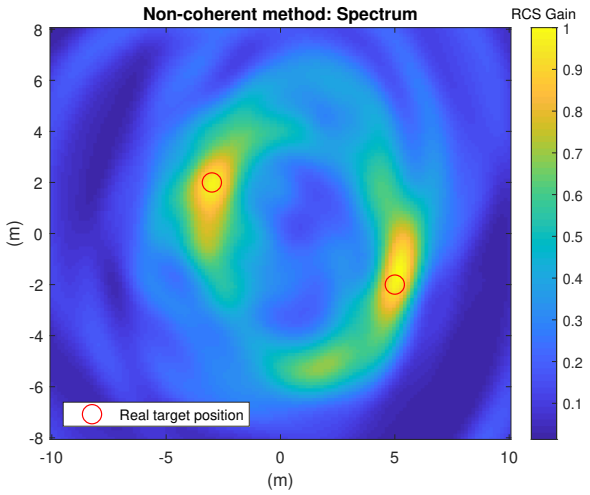

Figure 3.6: Non-coherent processing

Since the distance between both targets is much superior than the non-coherent resolution (see 3.2) , both targets are correctly detected.

From here on, to analyse the capabilities of the coherent method, two close targets (distance < non-coherent resolution) with the following space positioning will be considered:

Targets	**Position (x,y) (m)**
Target 1	(-0.02,-0.02)
Target 2	(0.02,0.02)

Table 3.5: Targets positions

3.2.2 Configuration 2 - Random Distribution of 4Tx/4Rx Antennas

The previous configuration works well for detecting targets separated by more than 1.5 m, however when two close targets are considered, some problems emerge. To prove so, we consider now another random space deployment of 4x4 transmitting/receiving antennas, but this time with two target only a few centimeters apart (see locations in table 3.5), as depicted in figure 3.7:

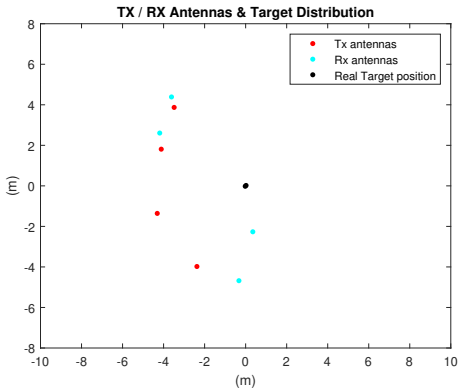

(a) Antennas and targets distribution: overview

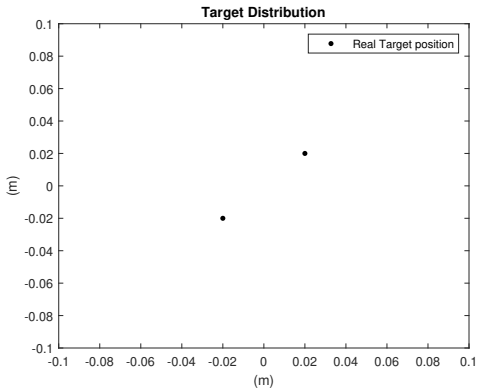

(b) Targets distribution: zoomed

Figure 3.7: Configuration 2 - antennas and targets distribution

Non-Coherent Processing

By applying the non-coherent processing algorithm the following heat map is given as the output:

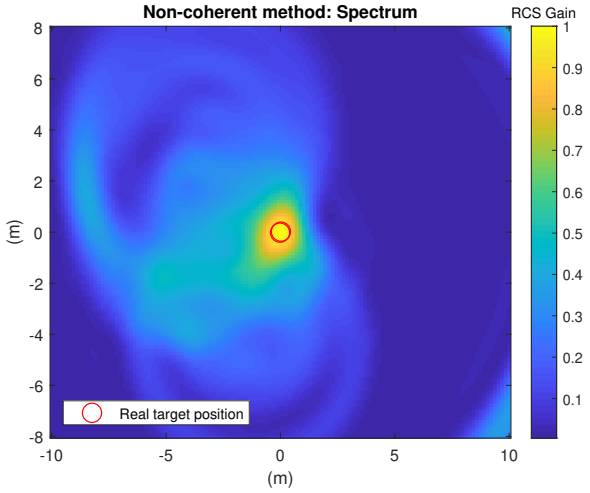

Figure 3.8: Non-coherent processing

Since the targets are within a distance from each other that is below the resolution of the coherent method (see 3.2), they are not discriminated by the non-coherent processing method, as it would be expected.

Coherent Processing

Considering now the coherent method, we see in the figure below that both targets are detected. Nonetheless, we can see some sort of noise around the processing window that can generate some false positives.

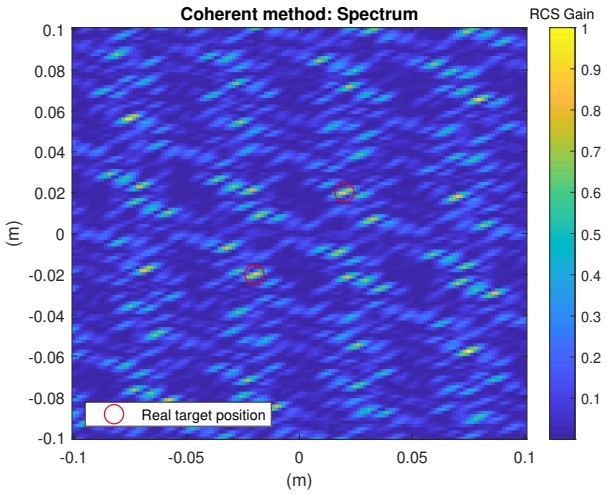

Figure 3.9: Coherent processing

This kind of clutter is also expected because random positioning of antenna arrays and their properties have been investigated and results have shown that the Mean Side Lobe (MSL) is inversely proportional to the number of antenna elements [5]:

$$MSL = \frac{1}{MN} \tag{3.4}$$

Knowing the relation between the number of antennas and the MSL, we can now analyse the coherent ambiguity functions in this scenario (considering a single target at origin):

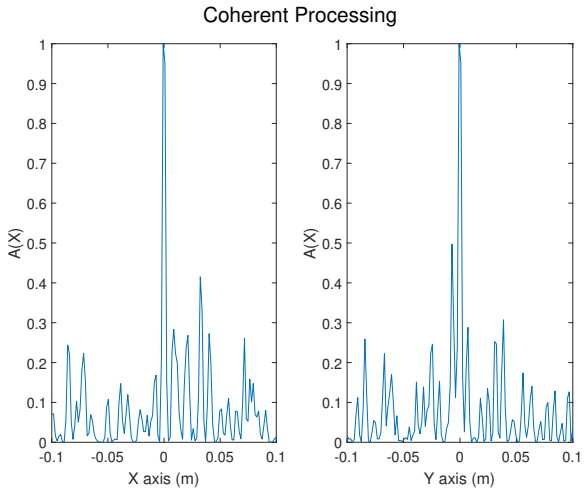

Figure 3.10: Ambiguity functions - coherent processing

As we can see in figure 3.10 , besides the MSL problem there are some Peak Side Lobe (PSL) that also interfere with the targets correct localization.

3.2.3 Configuration 3 - random distribution of 8Tx/8Rx antennas

In order to try to decrease the MSL in the coherent processing method, a different configuration is simulated. This time with an 8x8 randomly spaced antennas:

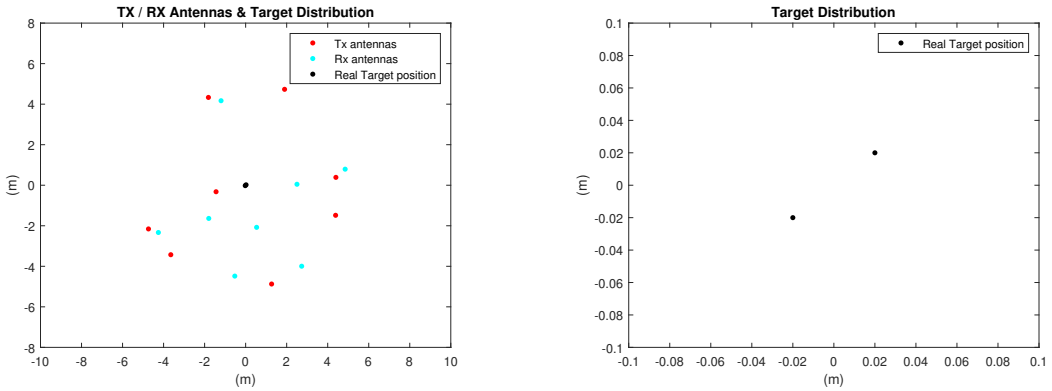

(a) Antennas and targets distribution: overview (b) Targets distribution: zoomed

Figure 3.11: Configuration 3 - antennas and targets distribution

With this configuration, we can obtain the following coherent heat map:

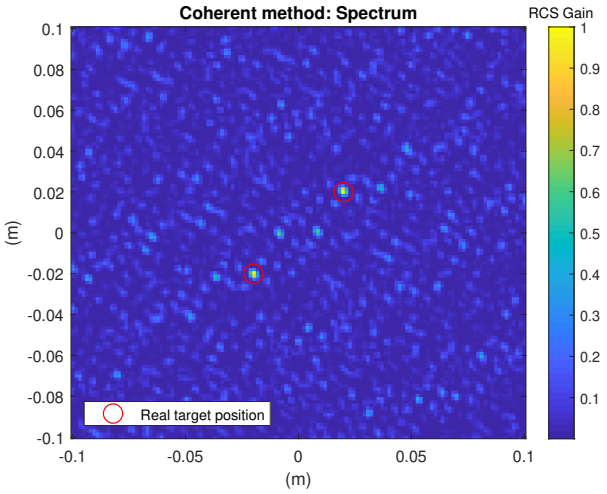

Figure 3.12: Coherent processing

By looking at figure 3.12 we can see that there is not much background noise, and this noise reduction can be explained by the increased number of antennas deployed and their relation with the MSL (see 3.4). By looking once again at the coherent ambiguity function (with one target at the origin), it is possible to have a better perception of this reduction:

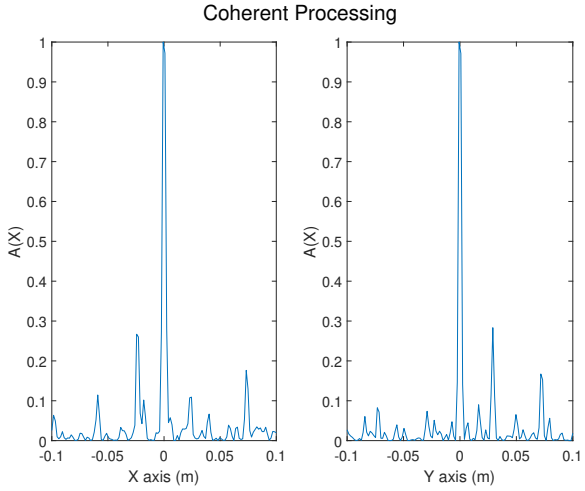

Figure 3.13: Ambiguity functions - coherent processing

According to the results presented in figure 3.13, we see that the MSL has decreased significantly making this configuration an excellent solution to correctly detect targets with a resolution of the order of wavelength (expression 3.3). However, this specific configuration is extremely hard to achieve in practice (more details in section 3.3 and in chapter 4), To overcome this problem, we need to get back to the 4x4 solution, but with different antenna configurations.

3.2.4 Configuration 4 - Distribution of 4Tx/4Rx antennas over two perimeter sides

In order to achieve a compromise between the hardware constraints and the best performance possible, some new configurations were simulated and analysed. This first configuration contemplates 4 transmitting antennas along the $(-10, y)$ line with a separation of 1 m and 4 receiving antennas along the $(x, -8)$ line also with a separation of 1 m:

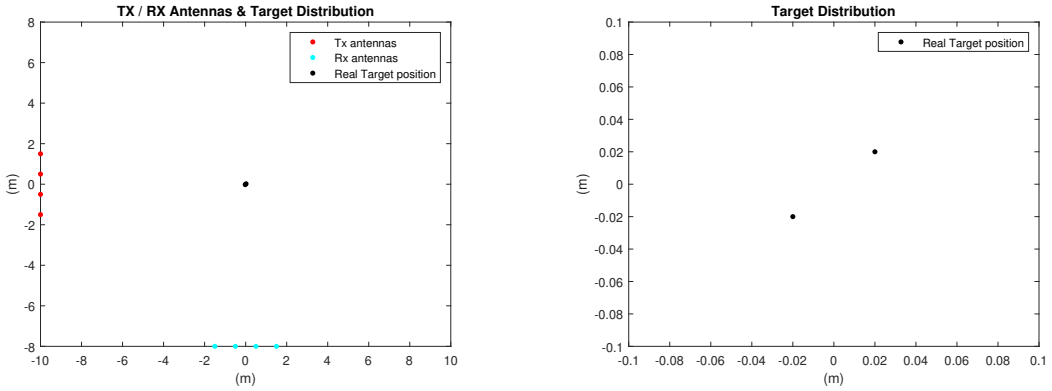

(a) Antennas and targets distribution: overview

(b) Targets distribution: zoomed

Figure 3.14: Configuration 4 - antennas and targets distribution

Coherent Processing

For this configuration, by performing the coherent processing, the following heat map is obtained:

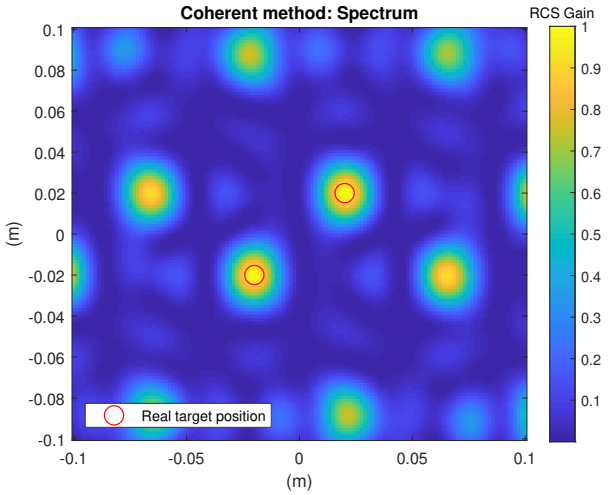

Figure 3.15: Coherent processing

After analysing figure 3.15 we see that both targets are well located, however, a repetition pattern is verified. The ambiguity function for this configuration is the following:

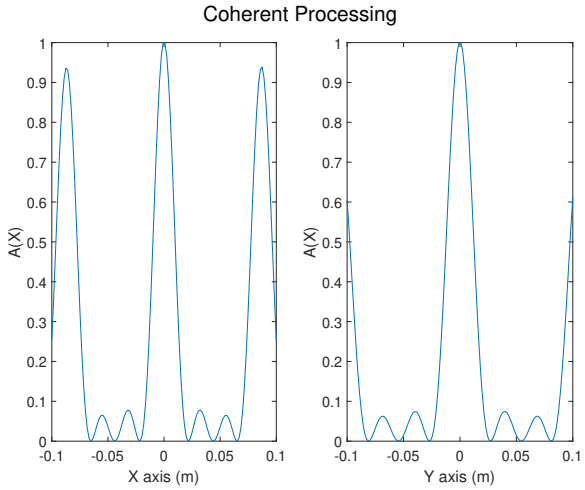

Figure 3.16: Coherent processing

From the ambiguity function we see that the pattern depicted in figure 3.15 is a consequence of the grating lobes observable in figure 3.16. These lobes are significant, leading to great interferences and false positives. In this scenario the antennas are uniformly distributed and sufficiently close to each other to be misled as phased-array antennas, however, since their separation is greater than the transmitting wavelength, some grating lobes are expected, as figure 3.16 proves.

3.2.5 Configuration 5

This last configuration is the result of the best compromise between performance and hardware limitations and its code can be found in appendix A. In this scenario, the antennas are disposed in 4 pairs of transmitters and receivers. These pairs are all aligned along the $(-8, x)$ line, with 5 meters of separation between pairs and 1 meter within each pair:

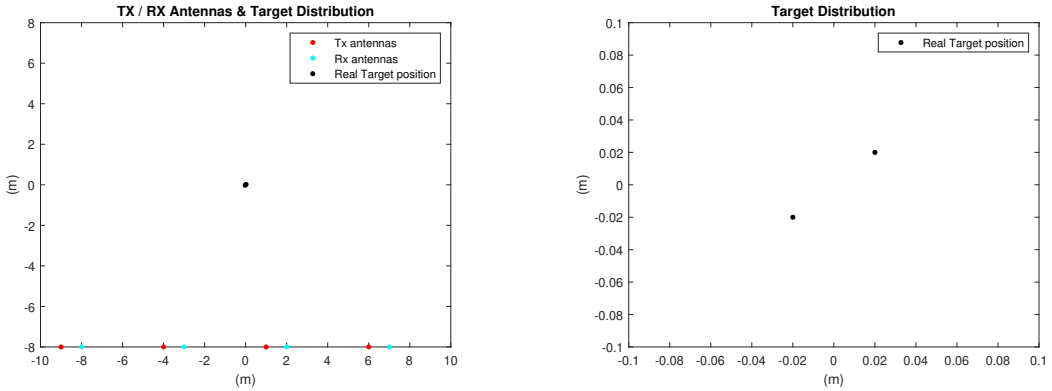

(a) Antennas and targets distribution: overview (b) Targets distribution: zoomed

Figure 3.17: Configuration 5 - antennas and targets distribution

So, with this last configuration, the output of the coherent method is then:

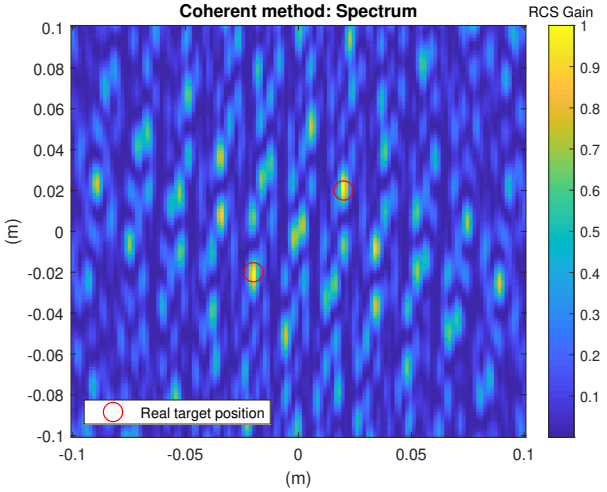

Figure 3.18: Coherent processing

After evaluating this output it is clear the improved performance in relation to the other configurations (except for 3.2.3, but this one is not achievable with the setup described in chapter 4). By checking the ambiguity functions, we see that, for this configuration, the grating lobes observed in 3.16 were suppressed, only remaining some residual side lobes and background noise:

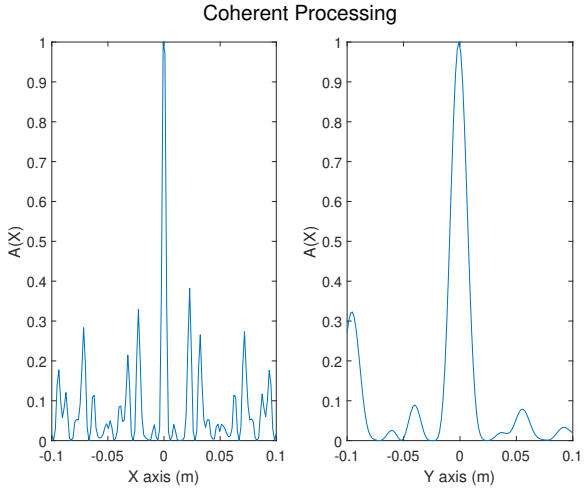

Figure 3.19: Coherent processing

3.3 Simulation Results Analysis

In this chapter, several possible configurations were presented and their outcomes are now interpreted and compared with more detail. These configurations were also a product of a parallel development with the experimental setup (details in chapter 4), thus the wide variety of scenarios considered.

In this way, after checking the correct behavior of the non-coherent processing method (section 3.2.1), a 4x4 random deployment was simulated to study the coherent processing method, however, the simulation results were not the best since the output had some undesirable side lobes (section 3.2.2). The first solution to this problem (following the $1/MN$ expression) was to increase the number of antennas. So, with an 8x8 random deployment (section 3.2.3) the coherent processing results were greatly improved (removing almost all the background side lobes). However, this scenario has different practical limitations, making it unattainable for the setup considered in chapter 4. Firstly, in these simulations the antennas are considered isotropic and no direct links between antennas are considered, as well as reflections. Given this, in a real life application, this specific random space deployment would be unreachable within the scope of this work. Also, considering the setup described in chapter 4 there are some hardware constraints that limit the number of antennas used (to 4 pairs of transmitter/receiver antennas).

So, with the 4x4 deployment limitation in mind, the configuration in section 3.2.4 was the first solution designed to overcome the background clutter described in section 3.2.2 and also to avoid direct links between the antennas (see section 4.8). This configuration solved the side lobes' problem, but at a cost of some grating lobes, causing significant interferences. In order to solve this grating lobes' problem, and because the best way to implement the setup was by grouping the antennas in Tx/Rx pairs, the final configuration was accomplished (figure 3.18). Despite not presenting the best performance between all the configurations, it contemplated the best results according to the setup limitations.

One important thing to take into account is the almost perfect simulation environment, regarding perfect transmitters/receivers/targets and no undesirable reflections. Although

the final configuration was planned to mitigate some of these limitations (by placing the antennas in the same axis), during experimental testing some placement adjustments might be necessary.

CHAPTER 4

Experimental Setup

In parallel with the simulation segment described in chapter 3, an entire system was studied and characterized. This system includes all the components needed to achieve a working prototype (from the antennas to the central processing unit). In this chapter, the RETIOT experimental setup is presented, with more focus on the subsystems developed by the author, namely, the optical link and RF amplifying stages. Besides these subsystems' characterization, the full integration and assembly of the whole setup are also demonstrated along the following sections.

4.1 Global overview

The experimental setup was designed so it can support four transmitting antennas and four receiving antennas, being all of them connected to a central unit through an optical link, as depicted in figure 4.1:

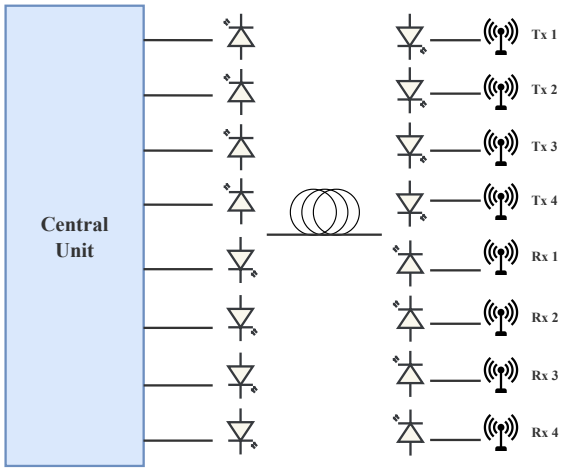

Figure 4.1: System high level overview

The setup design was studied simultaneously with the simulation phase, because the experimental setup, namely the optimum antenna placement, depends on the simulation results, thus they must be articulated with an achievable setup. So, in parallel with the simulation, the setup depicted in 4.2 is developed. This setup consists of a Software-Defined Radio (SDR) (central unit), a reference signal generator, several diplexers (to multiplex each transmitting signal with the reference signal), an optical link (composed of transceivers, optical multiplexers/demultiplexers and optical fiber) and several radar sites. Each radar site comprises a diplexer (to demultiplex the transmitting signal into the transmitting radar waveform and reference signal), two amplifier stages, a Local Oscillator (LO) based on a Phase-Locked Loop (PLL), an RF frontend (up/down converters) and two antennas. Besides engineering the whole setup, in figure 4.3, highlighted in green, are the components in which this work is more focused about.

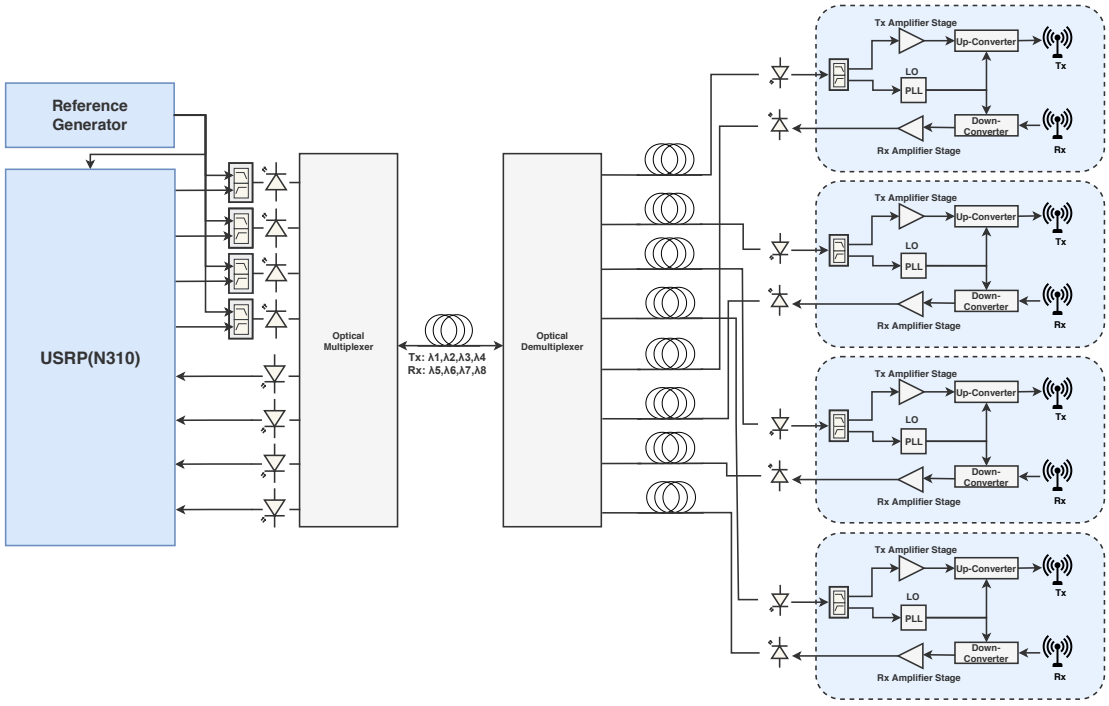

Figure 4.2: Detailed system overview

The detailed setup depicted in figure 4.2 represents the outcome of several iterations over the system development. Thus, it translates the best achievable solution that guarantees the phase coherence needed to perform coherent processing with a lower implementation cost (by distributing the same reference signal over the several radar sites). By pairing the transmitting/receiving antennas it is possible to decrease considerably the hardware components, i.e. one PLL can be shared for each pair of antennas, so only 4 are needed, instead of 8. Also, transmitting the reference signal needed for the PLLs would be difficult if the Rx antennas were separated from the Tx antennas. Thus, we see that by doing this resource optimization both complexity and cost of the system are reduced. These upgrades were always made in compliance with the simulation phase, in order to ensure that by pairing the antennas, good

results are achievable, guaranteeing a positive trade-off between performance and hardware optimization.

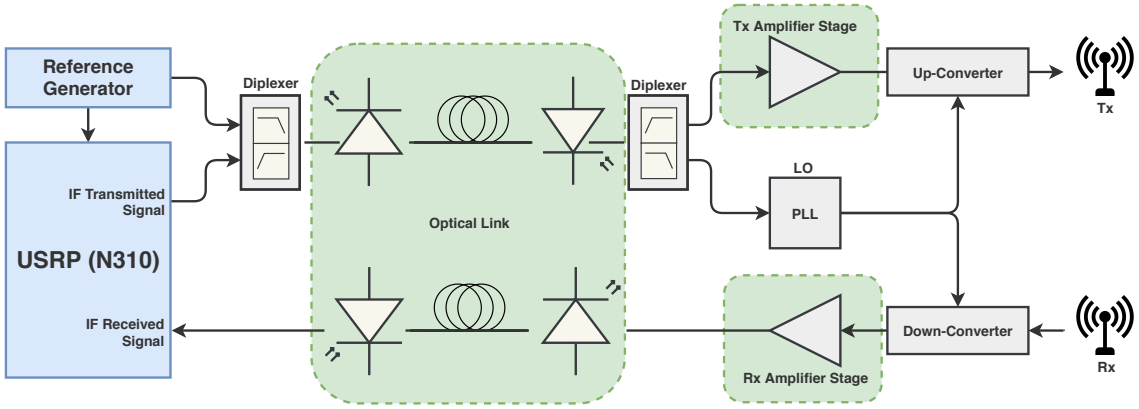

Figure 4.3: Single Radar site - diagram

To better understand how the setup works, it is preferred to analyse only one of the four antenna sites, as exposed in figure 4.3. In the down-link, the USRP USRP generates an Intermediate Frequency (IF) signal. Then, this IF signal is multiplexed (in frequency) with the reference signal through the diplexer. After, the multiplexed signals pass through the optical link all the way to the other diplexer, at the Radar site. Next to demultiplexing the signals, the reference signal feeds the local oscillator based on a PLL, whose output is used to up-convert the amplified IF signal to the radar frequency. The received signal is down-converted to the IF frequency using the same PLL output as the transmitter. The signal is then amplified and goes through the optical link all the way to the USRP, to be processed.

4.2 USRP

The central unit of the system is a Software-Defined Radio (SDR) based on a Universal Software Radio Peripheral (USRP) from *Ettus Research* (model N310). By using an USRP as the central unit, it is possible to have a flexible solution in terms of radio reconfiguration, since this technology is able to use the power of digital processing to move traditional hardware components such as filter, mixers or modulators to a malleable software solution.

Figure 4.4: USRP N310

This model has 4 Tx and 4 Rx single-ended channels with up to 100MHz of instantaneous bandwidth per channel and has a frequency range of 10MHz-6GHz. To maintain phase coherency between channels, an external oscillator is needed, however, this oscillator frequency range is limited to 600MHz-8GHz, and it is specified that the oscillator frequency must be twice the center frequency, limiting the center frequency range to 300MHz-4GHz. Therefore, the chosen IF is 3.84GHz. Also, the Tx channels have a maximum transmitting power of 18dBm and the Rx channels support signal power levels between -65dBm and -15dBm.

4.3 Power Splitter & Diplexers

In order to distribute the reference signal over the 4 Radar sites, a 4-way RF power splitter is required. The ZB4PD-52-20W-S+ splitter from *Mini-Circuits* is the one to use since it offers a great matching (1.1dB of VSWR), high isolation between ports (32dB) with a low insertion loss (0.3dB) and an excellent amplitude/phase unbalance of 0.1dB/1º, respectively. These characteristics are excellent to reduce losses and to guarantee the phase coherence among the components (because of the minor phase unbalances it produces).

The diplexers are passive devices with 3 ports: a high frequency port (with a high-band pass filter), a low frequency port (has a low-band pass filter) and a common port. In this setup, the diplexers act as a 2-way RF frequency multiplexer at the central unit side (multiplexes the IF and reference signal) and as a demultiplexer at the radar sites (separating the signals IF and reference signals). The ones used in this setup were developed *in-house* by the RF group and by measuring the gain for the high/low frequency ports in relation to the common port, it was concluded to have some minor insertion losses of 0.3dB for each port.

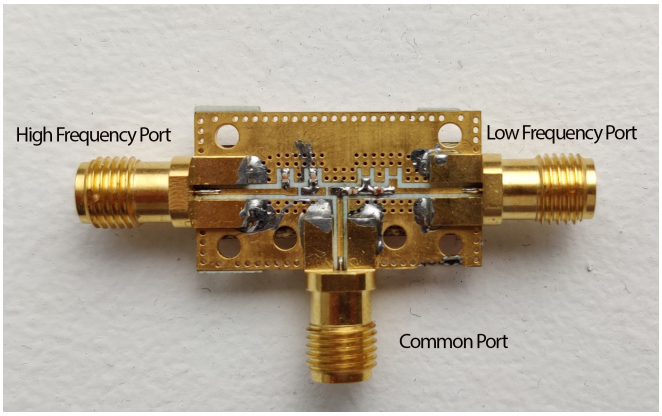

Figure 4.5: Diplexer

4.4 Optical Link

The RoF concept refers to the principle of transmitting a radio wave over a fiber link and this approach is the most attractive option to transport radio signals to and from the antennas, due to the fiber low attenuation and large bandwidth. So, as introduced in chapter 1, this concept is the one implemented in this setup in order to distribute radar signal in several widespread sites. As depicted in figure 4.6, the optical link is made up of 2 functional modules: the transceiver (which enables the Electrical/Optical (E/O) Optical/Electrical (O/E) conversions) and the fiber channel. Since this setup needs to transmit several signals the optical multiplexer/demultiplexer is added as the third module of the optical link, enabling the transmission of several wavelengths over the same fiber.

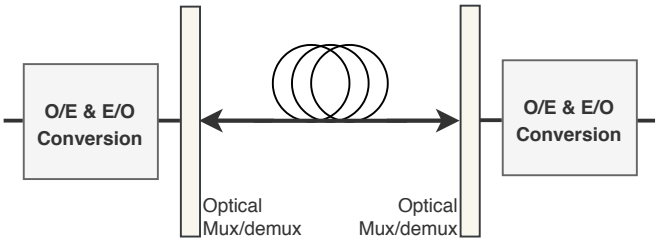

Figure 4.6: Optical link diagram

Optical Fiber

Starting to look into optical fibers, they can be classified as Single-Mode Fiber (SMF), which is designed to allow only the fundamental mode propagation or Multi-Mode Fiber (MMF), which allows the propagation of several modes for the same wavelength [20]. As a consequence of the different group velocities for each mode, MMFs have large modal dispersion, limiting both the link's length and transmission capacity. For this reason, MMFs are usually operated in short-range scenarios. On the other hand, due to their low dispersion, SMFs have been applied to a wider-range of operations with high-performance links. Thus, they are of great interest to be studied in this context and will be considered from now on.

Another important thing about the fiber channel is that although it provides a low-loss RoF distribution, inherent dispersion effects can be significant, being chromatic dispersion the most significant type in a SMF. As referred in [21], due to the fiber dispersion, the power of the electrical signal at the detector output varies according to the following expression:

$$P_{RF} \propto cos^2(\frac{\pi LD}{c_0}\lambda_c^2 f_{RF}^2) \tag{4.1}$$

where L is the fiber length, D is the dispersion, λ_c is the optical carrier wavelength, f_{RF} is the RF modulation frequency (RF signal). This expression shows the great impact that the frequency of the RF signal has on the P_{RF}. As an example, if the RF modulation frequency is of the order of 28GHz the signal at the detector would experience a deep fade after a few kilometers. To overcome this limitation, the transmission of the Radar signal over the optical link is made at an intermediate frequency (IF frequency of 3.84GHz) where the fading is negligible and the up/down conversion only happens at each Radar site.

Transceivers

Regarding the emitters and receivers, both O/E and E/O conversions are made by means of modified digital SFPs from *FiberStore* in order to be used as analogue optical transceivers (see previous work [22]). As seen in figure 4.7, these transceivers were modified by bypassing the digital circuitry of their boards. Thus, obtaining low-cost transceivers with a small form factor, which makes them a good choice to what this project demands (due to their small form factor, the evaluation board depicted in 4.8 is used).

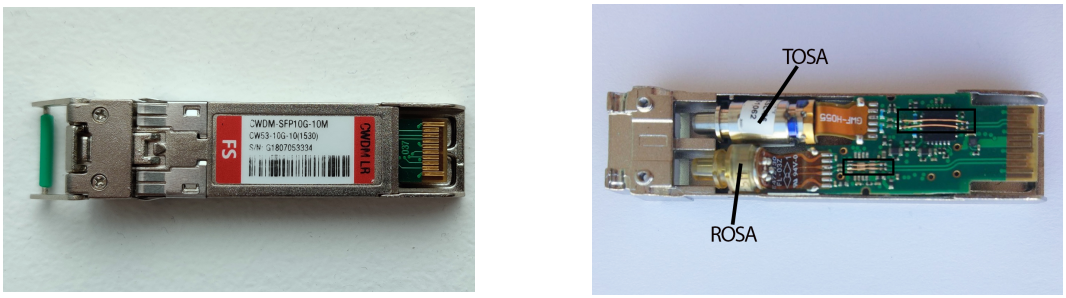

(a) (b)

Figure 4.7: Original digital SFP transceiver in a) and modified SFP transceiver in b) [22]

One important thing to mention is that these transceivers have differential RF ports to enhance the interference immunity of the system, but in this work, since the USRP channels are not differential, the single-ended operation is employed. Also, each SFP has a Transmitter Optical Sub-Assembly (TOSA) and a Receiver Optical Sub-Assembly (ROSA) incorporated (see figure 4.7), and as experimentally verified in [23] and [22], there are some crosstalk interferences between the transmitter and the receiver (due to both being on the same circuit board) that might be problematic. The crosstalk interference will be interpreted by the radar as a target at 0 distance, which will be ignored. However, we also have to make sure that this interference does not saturate the amplifiers at the receiver.

In this system, according to the setup depicted in figure 4.2, 4 SFPs at the USRP side and 1 SFP for each radar site are needed. As figure 4.16 demonstrates, next to the

USRP, 4 SFPs have the following Tx/Rx wavelengths(nm): 1470/1490, 1510/1530, 1550/1570, 1590/1610. From the radar sites side, the transceivers have the following Tx/Rx wavelengths(nm) :1490/1470, 1530/1510, 1570/1550, 1610/1590.

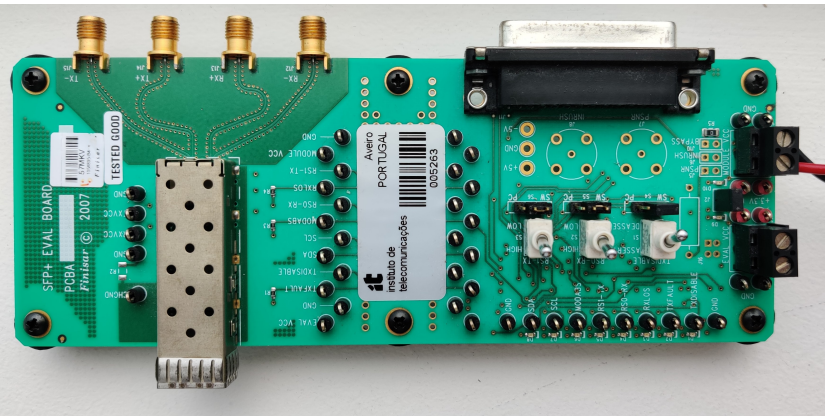

Figure 4.8: SFP evaluation board [23]

These transceivers are the critical part of the optical link because they are low-cost and were handily adapted in order to support RoF transmission. In this context, direct modulation is employed in these SFPs, so the linear region of the laser output power versus RF input current is a restrictive factor (see figure 4.9). The photodetector frequency response and non-linear conversion is also restrictive. As a result of these limitations, some drawbacks are expected and must be well characterized in order to perform the correct SFPs integration in the system. To do so, the characterization of the 1530 nm SFP is made, and its results are a representation of all wavelengths, since the 4 SFPs present have similar performance (experimentally verified in [23]).

FiberStore CW53-10G	
Transmitter λ_c	1530 nm
Transmitter Output Power	-5dBm up to 0dBm
Receiver Sensitivity	-14.4 dBm
Receiver Overload Power	0.5dBm

Table 4.1: SFP transceiver under-test: main specifications from datasheet

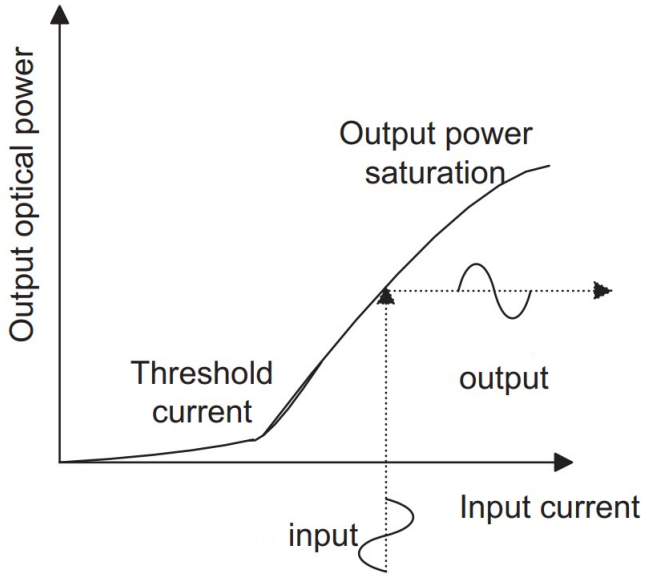

Figure 4.9: Typical transfer curve of a directly modulated laser [21]

The first measurement setup (figure 4.10) is made up of a Vector Network Analyser (VNA) that produces a RF signal frequency sweep to modulate the optical carrier generated by the laser from the TOSA. The modulated optical signal (transmitted with -1.7dB of optical power) goes through a single-mode fiber cable less than 1 meter long (so dispersion and attenuation become negligible), to reach an unamplified photodiode (Anritsu MN4765B) with 110GHz of bandwidth and a stable responsivity of 0.7 A/W, that does the O/E conversion and sends the RF signal back to the VNA.

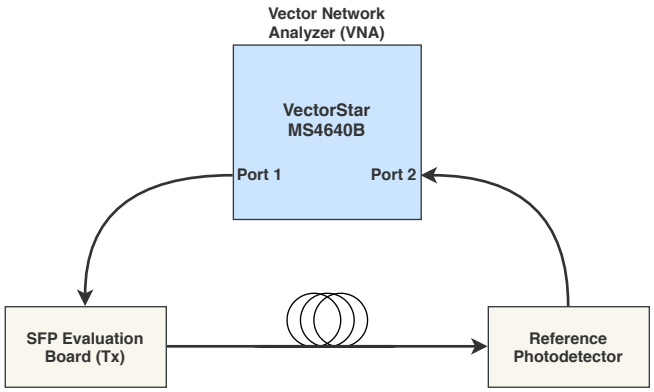

Figure 4.10: SFP Transmitter characterization setup

Following this measurement setup, several measures for different RF subcarrier power levels were made in order to check the transmitter behaviour. By analysing the results of figure 4.11a, we see that the laser is independent of the RF subcarrier power, however, its performance depends heavily on the RF subcarrier frequency (it gets worse as the frequency increases, up to 4.5GHz where its gain gets little improved). Also, we can verify the poor E/O conversion of the laser at the IF frequency (3.84GHz) by checking the losses of 40dB

to 45dB it introduces. Besides the high losses, there is also a poor input matching at the IF frequency, as depicted in figure 4.11a. The S11 represents how much power is reflected at the input, being S11=0dB all power reflected and S11=inf no reflected power (a good S11 value is less than -10dB, which is not the case).

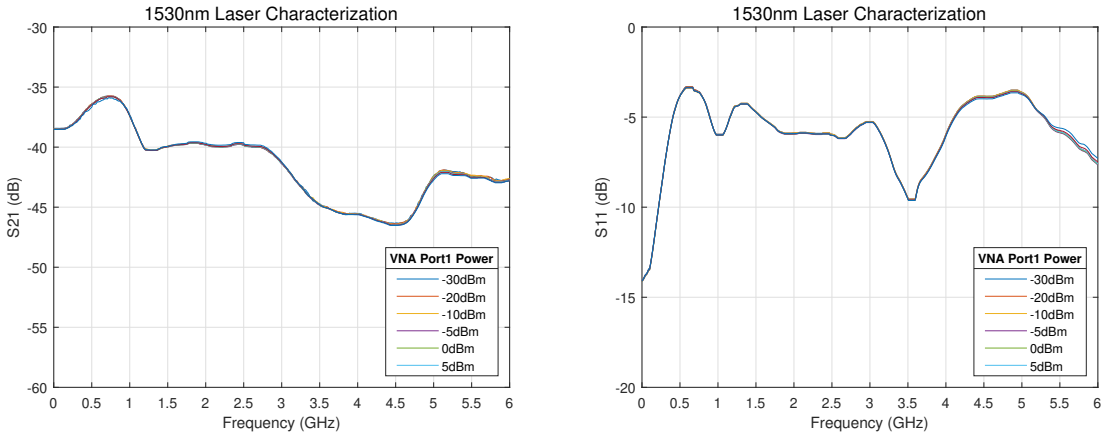

(a) (b)

Figure 4.11: SFP 1530 nm laser characterization

After describing the laser behaviour, the whole link characterization can be made. For this characterization, two setups are employed. The one in figure 4.12a uses two independent SFPs to avoid crosstalk, the one in figure 4.12b ensures the transmission and receiving of the optical modulated signal by the same SFP.

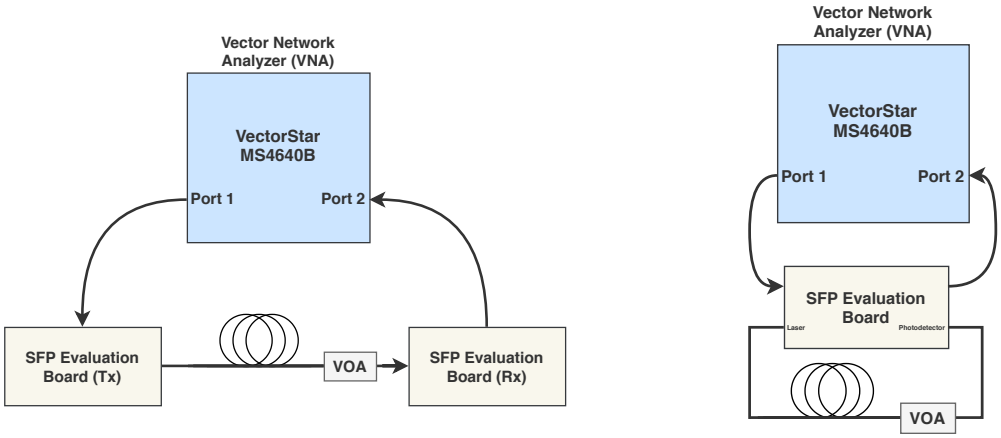

(a)

(b)

Figure 4.12: Optical link characterization setups

Regarding these setups, besides testing different RF modulation power levels, a Variable Optical Attenuator (VOA) is also used to test the link response to several optical power level at the receiver. From these tests, the following ones are the most relevant:

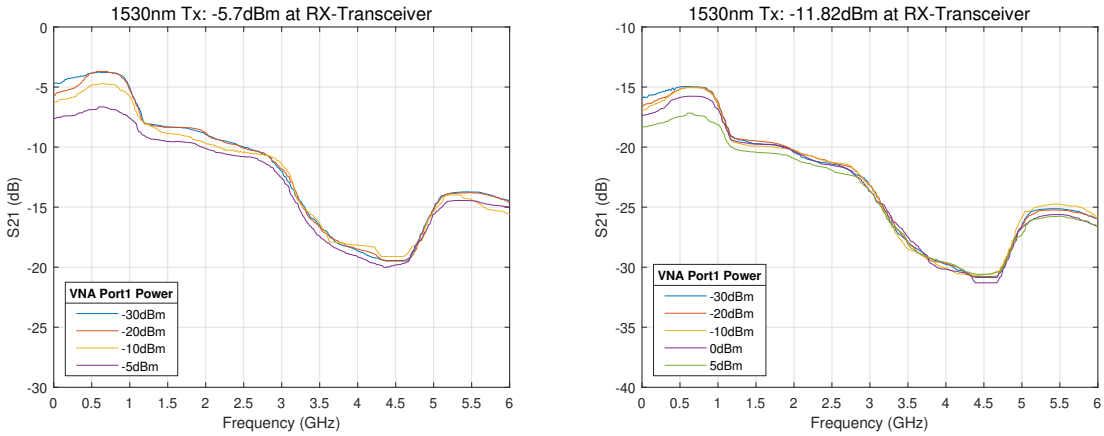

(a) (b)

Figure 4.13: 1530 nm - Optical link characterization using different SFPs

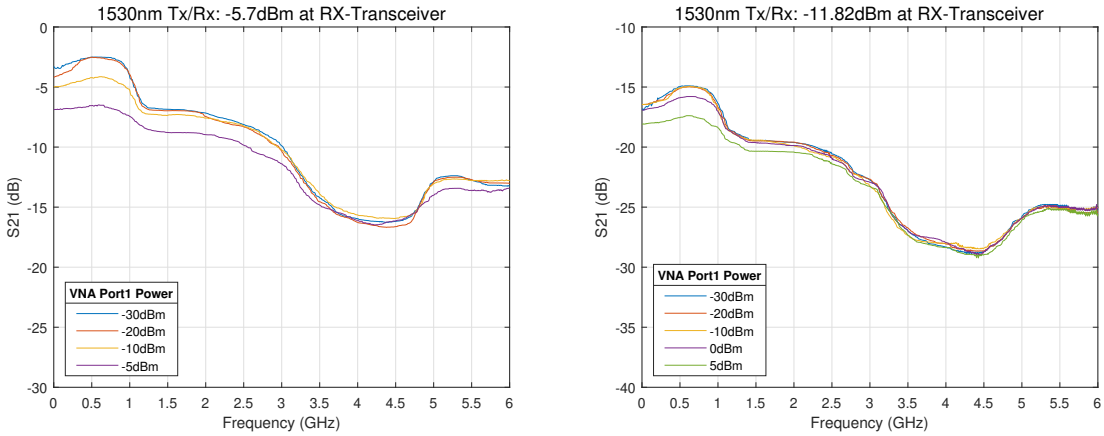

(a) (b)

Figure 4.14: 1530 nm - Optical link characterization using the same SFP

By directly comparing the results presented in figures 4.13a and 4.13b to the ones in figures 4.14a and 4.14b the crosstalk seems almost unnoticeable, since the results of both setups (figure 4.12) are really similar. However, an extra setup consisting of a VNA (to generate a 3.84GHz signal with several power levels) and a power meter (to measure the RF power at the receiver) was mounted to better analyse the crosstalk.

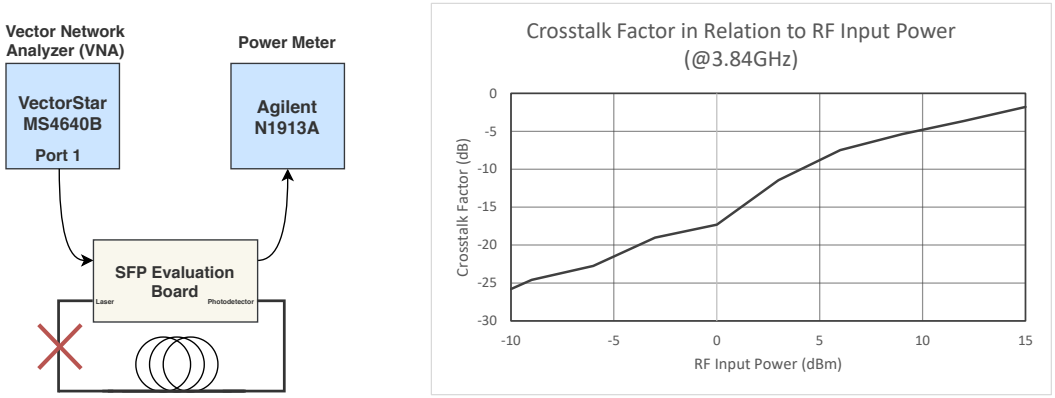

(a) (b)

Figure 4.15: Crosstalk analysis

By measuring the RF power at the receiver side with the laser on and with the laser off (optical link is cut, as the red 'x' of figure 4.15a represents), it is possible to get a measure of the crosstalk as a function of RF input power, in this work denominated crosstalk factor ($C_{factor} = \frac{P_{laserOff}}{P_{laserOn}}$). So, by analysing figure 4.15b we can verify that for this work's frequency spectrum and power levels, the crosstalk starts to have some impact for input power values above 0dBm.

Considering that the SFPs are meant to be used as both transmitters and receivers, the following analysis will be focused on figures 4.14a and 4.14b. At the ROSA photodetector, a photodiode converts the optical signal into an electrical current, being this current, in a linear regime, proportional to the power of the optical signal, being the proportionality constant called responsivity. The responsivity is related to the efficiency of the photodiode (i.e. how well it converts optical power into electrical current).

In both figures 4.14a and 4.14b we see that some distortions start to show up for higher RF input values. These distortions are mainly caused by the TOSA's integrated Transimpedance Amplifier (TIA) (after the photodetector), which is saturating. However, it is clear that for the high attenuated received optical signal (figure 4.14b), the TIA only starts saturating for an RF input power level of 0dBm, whereas for the low attenuated received optical signal (figure 4.14a) it starts with a lower RF input power level, -10dBm. This difference is explained by the O/E conversion at the photodetector because, for higher optical received signals, the photodiode produces a higher electrical current, thus the TIA gets easier saturated. Plus, the optical modulation process at the laser produces a constant optical component that is also converted into a DC current at the photodetector. This DC current might be saturating the TIA too (assuming an absence of a DC block between the photodiode and the TIA), however, since the TIA has a DC block at its output, it was not possible to determine if there is DC current flowing to the TIA or not.

In conclusion, the optical link presents a trade-off between attenuation and RF input power dynamic range (to have a better dynamic range more attenuated the signal gets, and vice-versa) and in section 4.9 the optimal solution is chosen to fit the system demands.

Optical Multiplexers/Demultiplexers

To multiplex and demultiplex optical signals, Coarse Wavelength Division Multiplexing (CWDM) technology must be used. This technology is a derivation of the standard WDM, which relies on a Thin-Filmed Filter (TFF) to perform the mux/demux of the optical signals. As light travels through several thin layers (with special optical properties) onto an optical-grade glass, its direction changes according to the light wavelength and the filter layers arrangement [24]. With the correct arrangement, several wavelengths can be multiplexed into a fiber, and vice-versa. The CWDM has a chromatic spacing of 20 nm, enabling relative high data rates at a low cost and with good transmission range (several tens of kms). Due to its generous chromatic spacing, it enable the use of low cost and un-cooled lasers, as the ones we have equipped in the SFPs, making this technology the best choice to this use case.

As a follow up of why the CWDM technology was chosen, the FMU-MC04E-A/B from FS is the optical multiplexer/demultiplexer to be used in this setup: Besides having a low Insertion Loss ($\leq 3.1dB$) and a good channel bandwidth for this application ($\pm 6.5nm$) this mux/demux is a passive device and is robust, so neither power supplies, cooling and special operating conditions are needed. Thus, we can have one mux/demux at the processing site and another one near the radar sites (as figure 4.16 depicts) to transport the 4 transmitting signals (mixed with the reference) and the 4 receiving signals over only one single-mode fiber cable.

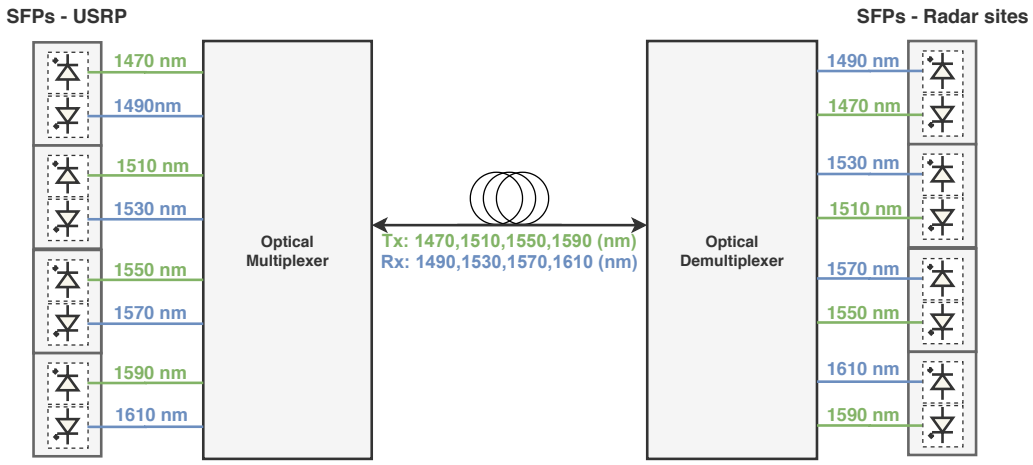

Figure 4.16: Optical multiplexing/demultiplexing - scheme

4.5 Amplifier Stages

One of the objectives of this work was also to develop amplifier boards to be integrated into the system, and so it was done. The goal was to develop some boards able to be implemented in both the transmitting/receiving sides. Thus, the choice of the amplifiers

ICs was made to establish a compromise between the power amplification needed for the transmitter and the low noise amplification needed for the receiver. In this way, and knowing the limitations regarding the IF (3.84GHz), *Analog Devices' ADL5611* and *ADL5240* were chosen. The following table has the most important features of these amplifiers: the gain; the 1 dB Compression Point (P1dB), which represents the output power level at which the gain decreases 1 dB from its constant value; the Third-Order Intercept Point (OIP3), which represent the output power that results in the imaginary interception between the linear amplification curve and its third order curve. The last two are important since they enable to check the saturation threshold of the amplifiers.

	Parameter @ 3.8GHz	**Value**
ADL5611	Gain	20 dB
	P1dB	17 dBm
	OIP3	27 dBm
ADL5240	Gain	19.6 dB
	P1dB	17 dBm
	OIP3	32 dBm
	Gain Control	31.5dB

Table 4.2: Amplifiers characteristics

The first amplifier (ADL5611) has a fixed gain of 20dB and the latter (ADL5240) is a Variable Gain Amplifier (VGA) with a 20dB gain internally matched amplifier and a 6-bit digital step attenuator with a gain control range of 31.5dB in 0.5dB steps. This attenuator adds a degree of flexibility regarding the integration of the amplifiers in the setup.

To have some room for manoeuvre in terms of gain, it was decided to design (using *Altium Designer* software), three different boards. Regarding the testing procedures, as with the characterization of the optical link, the same VNA was used to check the matching of the boards and their gain as a function of frequency and RF power. Figure 4.17 represents the measurement setup used to characterize all the three amplifier boards developed.

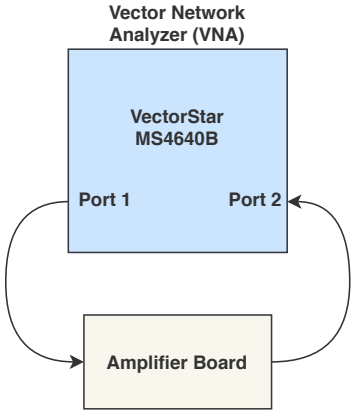

Figure 4.17: Board measurements setup

The first amplifier board consists of a single *ADL5611* amplifier, and the result of its design is depicted in 4.18:

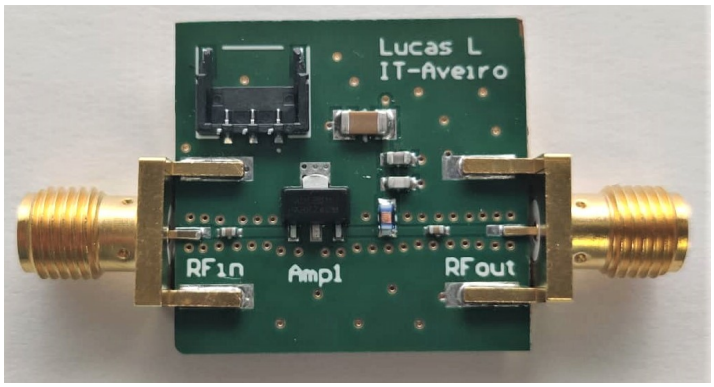

(a) ADL5611: Board

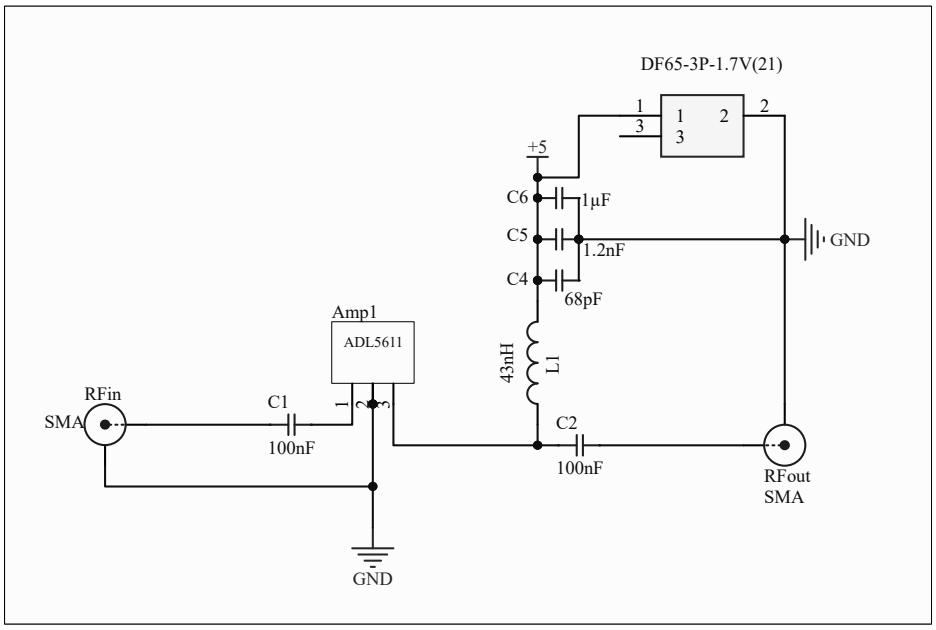

(b) ADL5611: Schematic

Figure 4.18: First board

As we can see from the board schematic (figure 4.18b), we have in series with port 1 an DC decoupling capacitor. Also, in port 3, we have a bias tee, which enables the supply of the DC voltage needed for the amplifier. The inductor L1 separates the supply DC voltage from the DC+RF signal at amplifier port3 whereas C2 makes the AC coupling, separating the DC+RF signal from the RF signal at the output. C4,C5 and C6 are decoupling capacitors meant to keep a stable supply voltage. The DF65-3p-1.7V(21) is the connector used for energy supply.

Running the measurement procedure (figure 4.17), the following relevant parameters were obtained:

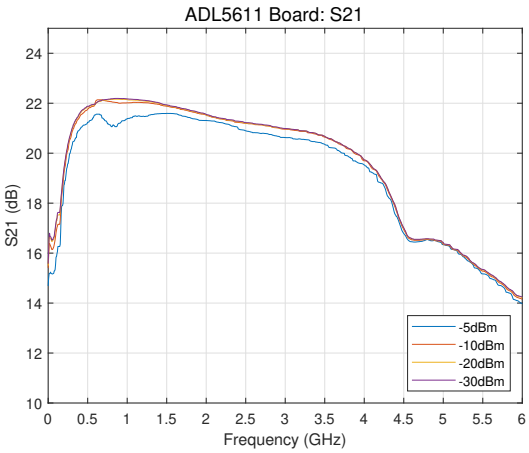

(a) ADL5611: S21

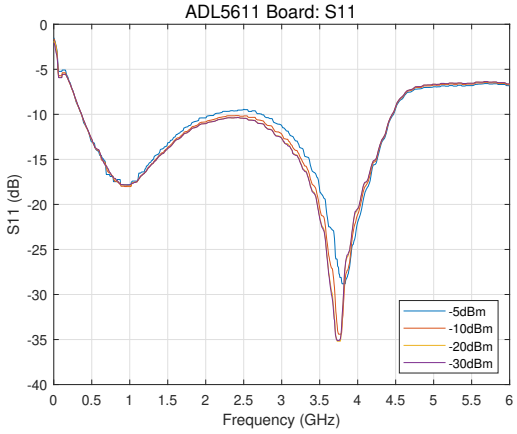

(b) ADL 5611: S11

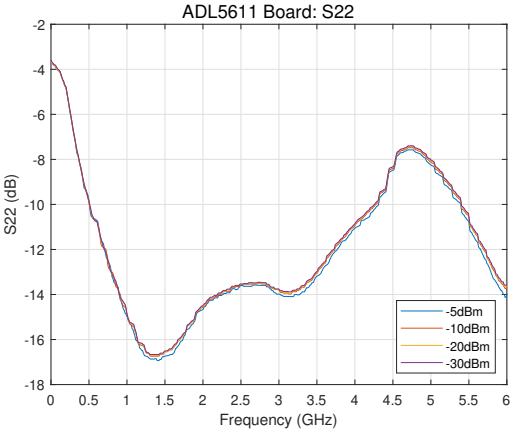

(c) ADL 5611: S22

Figure 4.19: ADL 5611 Board - characterization results

As we can see through figure 4.19a, the gain curve (S21) is approximately flat until 4GHz and at the frequency of interest (3.84GHz), this board behaves as expected, since it provides a gain of 20dB of the 21dB expected from the datasheet (see table 4.2). When the input power is -5 dBm, some saturation starts to be noticeable, but it is expected since its correspondent output is near the P1dB of the amplifier. In terms of matching, by inspecting figures 4.19b and 4.19c we can conclude that both input and output are well-matched($|S11|, S22 < -10dB$), i.e. there are no significant losses from undesirable reflections in both ports.

The second board (depicted in figure 4.20) has two *ADL5611* amplifiers in series, so it is expected to double the gain.

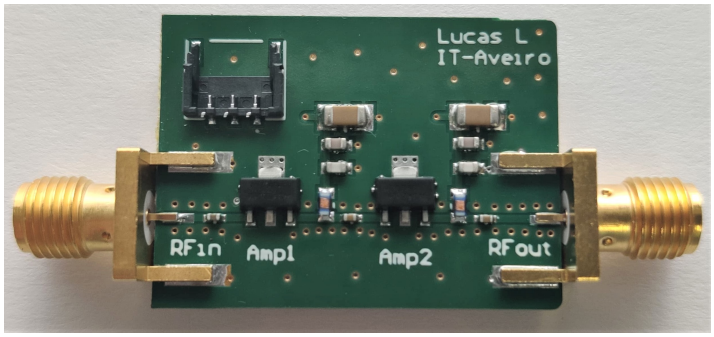

(a) Two ADL5611 in series: board

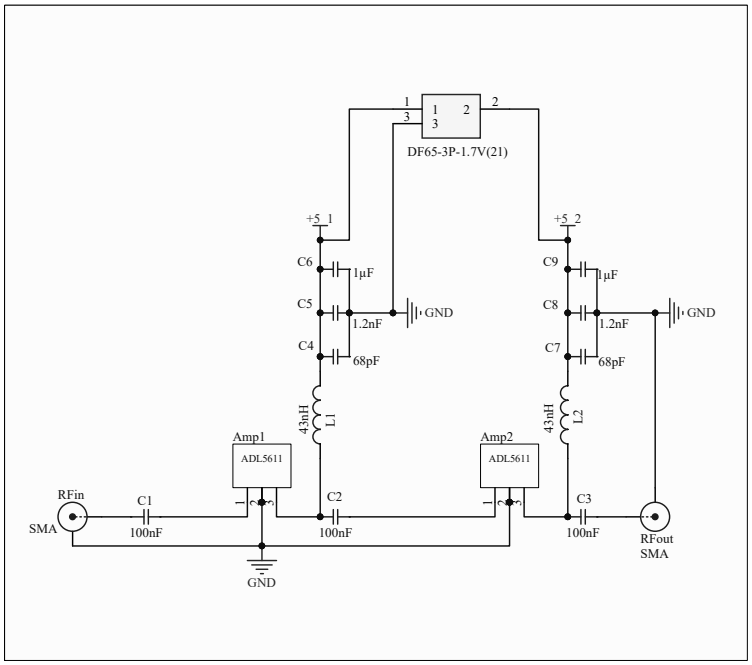

(b) Two ADL5611 in series: schematic

Figure 4.20: Second board

Regarding the board circuitry, this board is the same as the previous but with twice the components, so the explanation given before also applies for this board. In terms of characterization, from the previous board, we got good results in terms of port matching, so by placing another ADL5611 does not reproduce in significant differences. Thus, in this case, the relevant parameter is only the gain (S21):

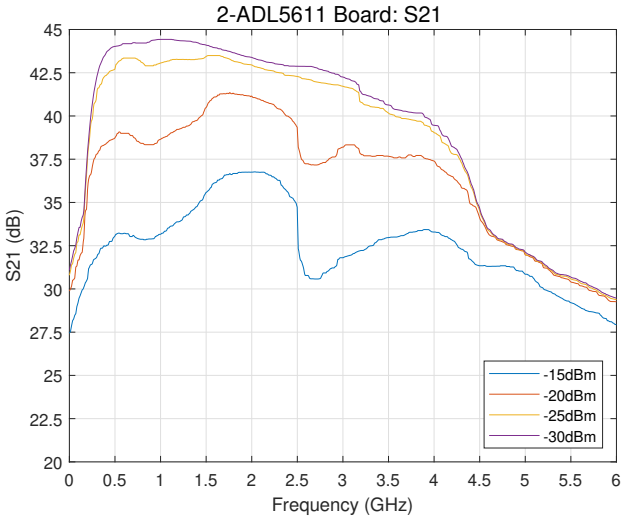

Figure 4.21: Two ADL5611: S21

By carefully analysing figure 4.21 we see that there is a lot of discrepancies between the curves. As mentioned in the analysis of figure 4.19a, we started to see a saturation with a -5dBm RF input power, so, by adding an extra ADL5611 in series with 20dB gain, it is expected for this saturation to start with $-5dBm - 20dB = -25dBm$, which is experimentally proved with this second board. Besides this limitation, this board behaves as expected, with a 40dB gain at the IF frequency.

Finally, figure 4.22 depicts the third board. As we can see, the board has two *ADL5611* in series with the *ADL5240*.

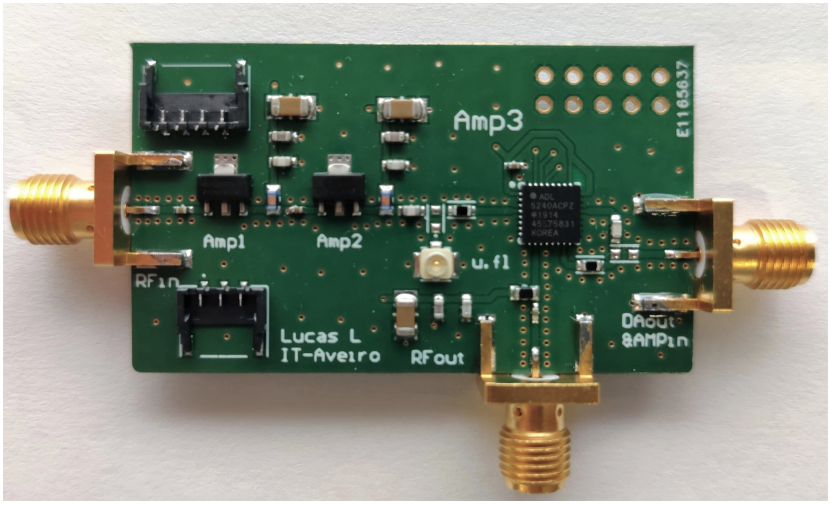

(a) 2-ADL5611 + ADL5240 in series: board

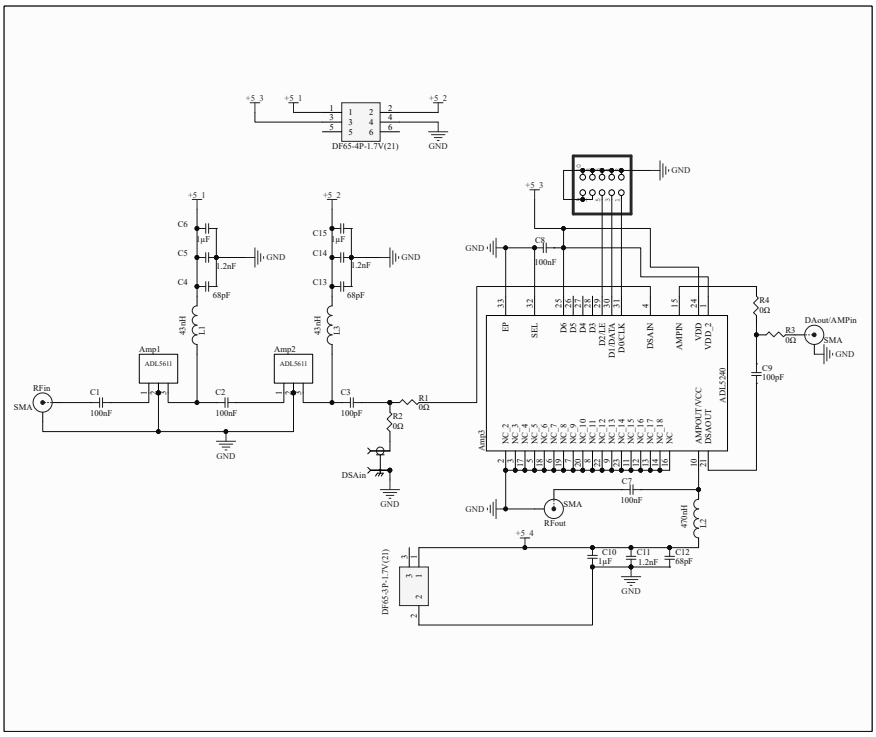

(b) Two ADL5611 + ADL5240 in series: schematic

Figure 4.22: Third board

By adding the ADL5640, some more complexity to the board was introduced. This variable gain amplifier, represented as the final big block in figure 4.22b, consists of a digital step attenuator in series with an amplifier. By configuring the attenuator to be prior to the amplifier, we get some more flexibility to control undesired saturation at the amplifier. The ADL5240's *attenuator-amplifier* diagram can be seen in figure 4.23:

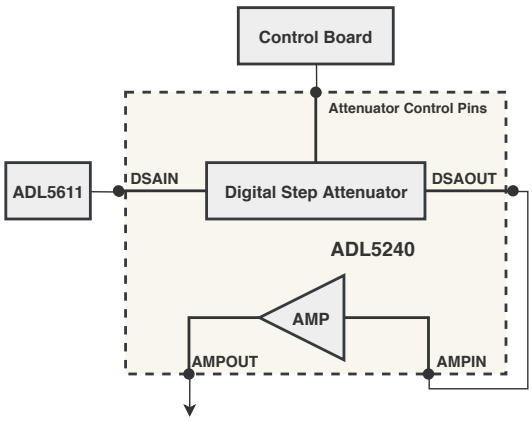

Figure 4.23: ADL5240: attenuator and amplifier diagram

Between the output of the second amplifier and the input of the attenuator, we have an extra RF strip and two 0Ω resistors whose purpose is for debugging (in case of some problem, we can play with the resistors in order to test only the first two amplifiers or only the third one). Regarding the ADL5640, between the attenuator and the amplifier input, it was also added another debugging point, so we could have the possibility to check only the attenuation/amplifier stages of the VGA. In terms of energy supply, the VGA has two separate port to supply energy for both the amplifier and the attenuator. In order to prevent some interferences, it was decided to separate all the DC inputs. As with the ADL5611 amplifiers, the ADL5240 also as the AC coupling capacitor at its input port and a bias tee at the output port. With this board, the S11 measurement is irrelevant because since it is relative to the ADL5611, the same amplifier used in the first board (and it is well-matched). However, with this new ADL5240 as the final stage of amplification, we can analyse the S22 of this board to check the ADL5240 output matching as well.

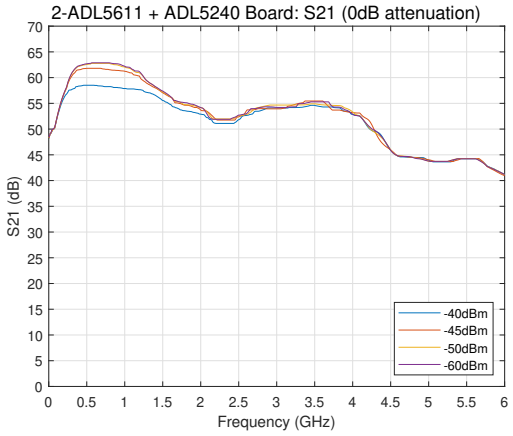

(a) 3 Amplifiers board (0dB attenuation): S21

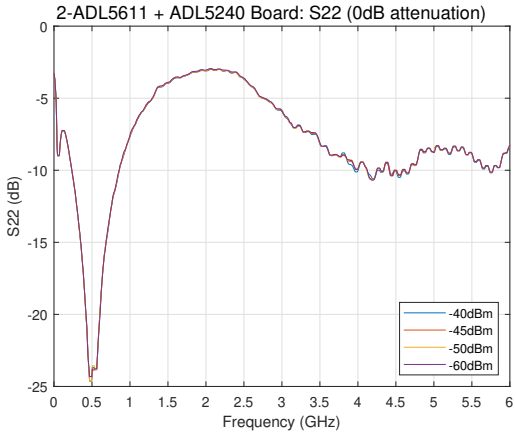

(b) 3 Amplifiers board(0dB attenuation): S22

Figure 4.24: 2-ADL5611 + ADL5240 Board (0dB attenuation): characterization results

From figure 4.24a we see that the total gain of the board is 54dB. By looking at table

4.2, by summing up the gains of the two ADL5611 plus the gain of the ADL5240, the total gain should be around 60dB. The difference between the experimental and expected results can be explained by some poor impedance matching at the output ($> -10dB$). Following the same saturation problem described in the commenting of the previous boards' results, With -45dBm of input RF power ($-5dBm - 20dB - 20dB - 20dB = -45dBm$) we can start to see some non-linear behaviour. This could be a potential limitation for the system and is better interpreted in section 4.9.

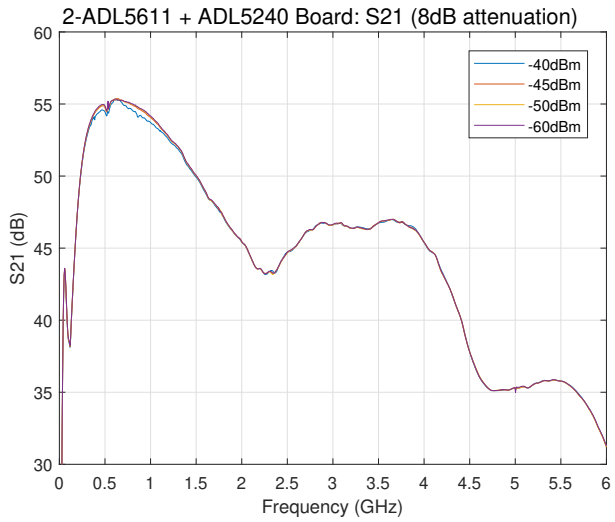

Figure 4.25: 3 Amplifiers board (8dB attenuation): S21

Figure 4.25 demonstrates the results of a possible solution to mitigate the saturation problem, which is the use of the attenuator embedded in the ADL5240 chip. By performing an attenuation before the last amplification stage, we can control the saturation issue at the cost of a lower amplification gain. This real time attenuation of 31.5dB range in 0.5dB steps is made through an SPI link between the amplifier board and a control board, which was developed and tested *in-house*. The control board also provides the attenuation control via wireless (smartphone App or Desktop).

4.6 RF Frontend

This setup has two RF frontend boards for each Radar site, one up-converter and one down-converter. These boards are designed to work with a RF signal of 28GHz (with 5GHz of bandwidth) and are based on a heterodyne architecture. Therefore, considering the frequency of the IF signal generated by the USRP (3.84GHz) and knowing that the mixer embedded in the board uses the 2nd harmonic of the LO signal, its frequency must be:

$$f_{LO} = \frac{f_{RF} - f_{IF}}{2} = \frac{(28 - 3.84)GHz}{2} = 12.08GHz \tag{4.2}$$

So, by using the same LO (see section 4.7 for generation details) for both up/down converters, phase coherence between transmitted and received signals is achieved.

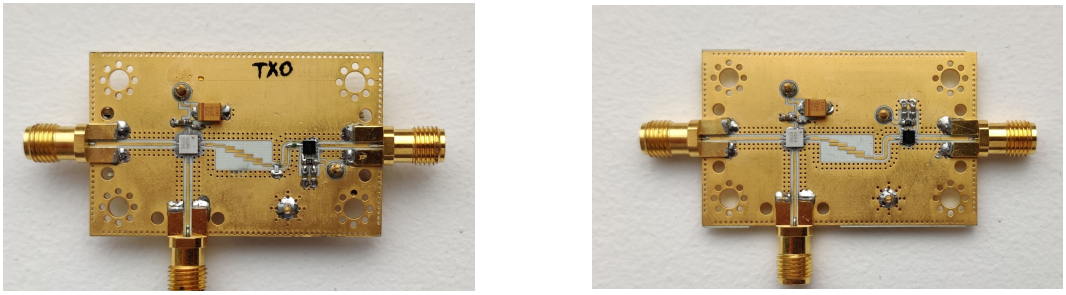

(a) Up-converter (b) Down-converter

Figure 4.26: RF frontend boards

All the details in this implementation can be found in [25] (note that this paper describes this exact system, but regarding boards with 4 replicas of the up/down converters depicted in figure 4.26). From the characterization done in [25], the conversion gain, and its correspondent limitations are highlighted in table 4.3:

	Parameter @ 28GHz	**Value**
Up-Converter	Gain	-1 dB
	P1dB	11 dBm
	OIP3	8.6 dBm
Down-Converter	Gain	4 dB
	P1dB	-3 dBm
	IIP3	4.4 dBm

Table 4.3: RF frontend: conversion gains

4.7 LO based on a PLL

To generate the LO signal needed for the up/down conversions, the LMX2595 evaluation board is used. This wideband synthesizer can generate frequencies from 10MHz to 20GHz and relies on a high performance PLL to guarantee phase synchronization between the 10 MHz system reference and its outputs, with low phase noise and jitter. As depicted in 4.27, this board has two differential outputs (RFoutAP/AM and RFout BP/BM) and a differential oscillator input (OSCinP/M), however, single-end operation is considered.

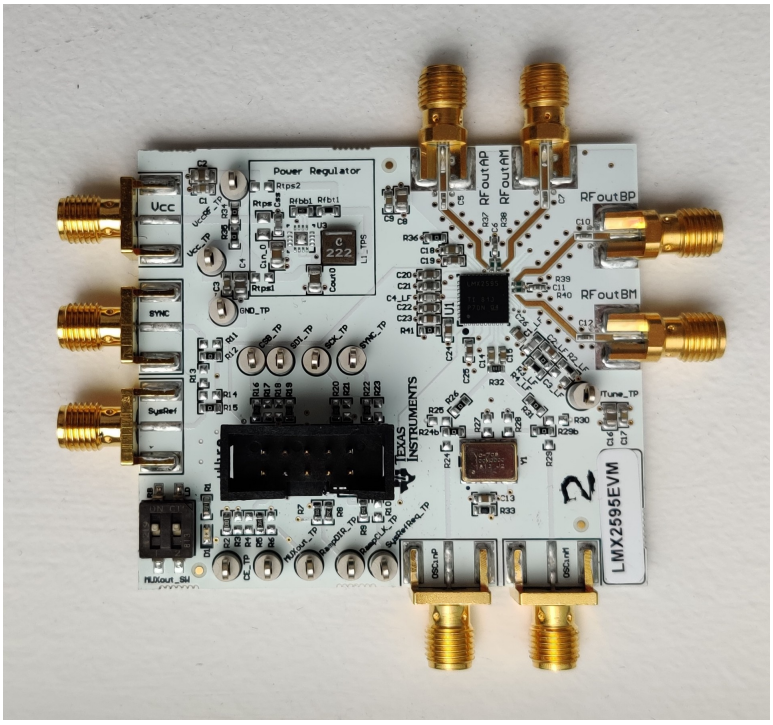

Figure 4.27: LMX2595 - evaluation board

As the scheme represented in figure 4.2 demonstrates, each Radar site has one of these boards, which is programmed to receive the 10 MHz clock from the optical link (over a range of -30dBm to 10dBm) and generate two phase synchronous 12.08GHz outputs (3dB maximum power) that feed both the up/down-converters.

4.8 Antennas

The antennas used in this setup are A-Info LB-180400-KF horn antennas that operate from 18GHz-40GHz. However, due to the potential of jointly have radar and communication capabilities, it was chosen to operate in the 5G millimetre wave frequency of 28GHz, which according to expression 3.3 is also a great frequency to achieve super-resolution in target detection. Therefore, making this system ready to jointly achieve target detection and 5G communication.

Figure 4.28: A-Info LB-180400-KF horn antenna

According to the datasheet, we can achieve a gain of 15dBi with a half power beam-width of about 27º in the E-plane and 25º in the H-plan. These characteristics are very important since the simulation model considers isotropic antennas with no direct links between them. Thus, knowing the characteristics of the antennas to be used in the experimental setup was one of the key points to achieve the final antenna configuration considered in simulation (see 3.2.5).

4.9 System Integration

With all the components described, an important step is to integrate them into the setup, and characterize the system as a whole.

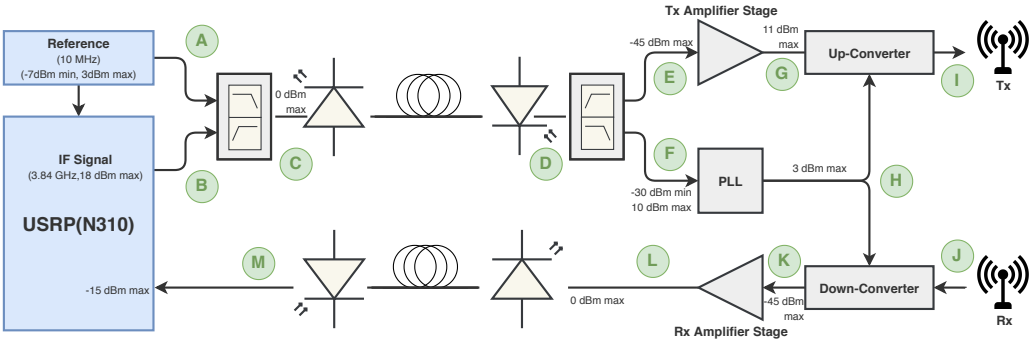

Figure 4.29: Setup power budget

The reference generator can generate the 10MHz reference signal with -7dBm to 3dBm of power. This signal is then distributed across 4 transmitting channels by passing through a 4-way splitter. The 4-way splitter divides the power of the signal into 4 so, each one of the outputs will have -6dB of power in comparison with the input minus 0.6dB from insertion loss. Considering the output of the reference generator as 0dBm, after being split into 4 reference signals, each one of them (point A) will have the following power:

$$A_{Power} = 10log_{10}\left(\frac{10^{0/10}}{4}\right) - 0.6 = -6.6dBm \tag{4.3}$$

Each reference signal is then multiplexed with the IF signal as they pass through the diplexer. This diplexer introduces a minor loss of 0.3dB in the multiplexing process (between points A/B to points E/F the system as two diplexers, so the total diplexer loss is 0.6dB). Between point C and point D the transmitting signal travels through the optical link (both transceivers, the mux/demux and also the fiber cable). This section is critical, mainly because of the attenuation introduced by the low-cost transceivers. According to section 4.4, when considering a high optical power at the detector (figure 4.14a) although having minor losses there is the limitation of -20dBm of RF input power as the saturation threshold of the detector. When considering the -11.82dBm optical signal at the photodetector (figure 4.14b), the RF input power saturation threshold is higher (0dBm), at the cost of a higher optical link attenuation. Since there is the power limitation of the reference generator (-7dBm to 3dBm) the latter scenario (-11.82dB of optical signal power at photodetector) must be followed. So, from figure 4.14b we can check that the optical link will have an attenuation of -16.5dB for the reference signal and an attenuation of -28.5dB for the IF signal. Plus, the optical mux/demux introduces 3.1dB of insertion loss and the fiber losses are negligible. Table 4.4 demonstrates the attenuation that both reference and IF signals are subjected to:

	Power at Points A/B	**Attenuation Diplexers**	**Attenuation Optical Link**	**Power at Points F/E**
Reference Signal	-6.6dBm	0.6dB	16.5dB+3.1dB	-27.1dBm
IF signal	-11dBm	0.6dB	28.5dB+3.1dB	-43.2dBm

Table 4.4: Signal attenuation over setup

Regarding each Radar signal, the goal is to have the maximum possible power radiated because of the high losses associated with the *over the air* transmission so the amplifier with 3 stages is the indicated (figure 4.22a) to amplify the signal at the IF frequency. However, this amplifier starts to saturate with -40dBm of input power. For this reason, it was chosen to generate the IF signals with -11dBm at the USRP (table 4.4) so that after being attenuated by the optical link, the signal had a power level below the saturation point of the amplifier board (although the USRP can generate signals with up to 18dBm signals, they would be heavily distorted by both optical link and amplifier, as analysed in the previous sections). The reference signal power is also below the distortion threshold of the optical link (0dBm) and, after passing through it, it feeds the PLL, which produces the oscillating signal necessary for the RF frontend.

	Power at Point E	Amplifier Gain @ IF Frequency	Power at point G
IF Signal	-43.2dBm	55dB	11.8dBm

Table 4.5: IF signal amplifier gain

Table 4.5 represents the gain provided by the amplifier board with 3 stages (see 4.22a) at the frequency of interest (3.84GHz). After the amplifier stage, the IF signal is up-converted to the Radar frequency (28GHz), suffering an attenuation of 1dB resulting in a 10.8 dBm Radar signal (point I) that is fed to each transmitting antenna (according to table 4.3, 11.8dBm is in the saturation limits of the up-converter, and taking into account the high PAPR of the OFDM signal (details in section 2.2.2) some adjustments might be done during experimental measurements. These adjustments might be the amplifier board gain adjustment in order to be under the saturation threshold of the up-converter.

Regarding the path loss associated with the *over the air* transmission of the Radar waveforms, we can use the known Radar equation of a monostatic system[2][26] to estimate the losses for the best and worst scenarios:

$$P_r = P_t + 2G + \sigma + 10log_{10}\left(\frac{c_0^2}{(4\pi)^3 f^2}\frac{1}{R_1^2}\frac{1}{R_2^2}\right) \tag{4.4}$$

being P_t the transmitting signal power (10.8dBm), $2G$ the Tx and Rx antennas gain (15dBi for both, since they are equal), σ the target's RCS (represents how well the target reflects the radar waveform), R_1 the distance from the transmitting antenna and the target and R_2 the distance from the target to the receiving antenna.

So, considering a target with a unitary RCS ($\sigma = 0dB$), the scenario of the last simulation configuration (see figure 3.17) and approximating the targets position to (0,0) we can estimate the received signal power (P_r) for the major loss case (Tx antenna position: -8,-9; Rx antenna position:-8,7) and for the minor loss case (Tx antenna position: -8,1; Rx antenna position:-8,2). For the worst scenario, expression 4.4 is substituted for:

$$P_r = 10.8 + 15 + 15 + 10log_{10}\left(\frac{c_0^2}{(4\pi)^3 28e9^2}\frac{1}{12^2}\frac{1}{10.6^2}\right) \simeq -74dBm \tag{4.5}$$

For the best scenario, the received signal power is estimated to be:

$$P_r = 10.8 + 15 + 15 + 10log_{10}\left(\frac{c_0^2}{(4\pi)^3 28e9^2}\frac{1}{8^2}\frac{1}{8.2^2}\right) \simeq -68dBm \tag{4.6}$$

Thermal noise is approximately AWGN and is the main noise factor in electronic systems and it is important to understand its influence at the receiver side of the system in order to correctly detect targets. Following the thermal noise power expression proposed by Nyquist:

$$P_{ThermalNoise} = 10log_{10}(kTB)(dBW) \tag{4.7}$$

being k the Boltzman constant ($k = 1.3807 \times 10^{-23} J/K$), T the ambient temperature (294K) and B the bandwidth (Hz). According to this expression, the thermal noise power of this

particular system can be estimated, considering the 5GHz bandwidth of the band-pass filter of the down-converter as the limiting bandwidth:

$$P_{ThermalNoise} = -106dBW = -76dBm \tag{4.8}$$

By comparing the thermal noise (as noise floor) to the signal receiving power for the worst scenario (expression 4.5) we can estimate a margin of only 2dB between them. Naturally, there are other random noise sources and losses that are not considered and that degrade even more the SNR at the receiver. Yet, since each receiver antenna receives signals from 4 different widely distributed transmitters, the SNR gets inherently increased. Besides, by feeding the matched filter with a mean value of several measures the SNR gets even better maximized. The noise component might also be reduced by digitally filtering the received signal at the central unit. Another important point is that for expression 4.4, a unitary target RCS was considered. This property is extremely complex and depends on several factors, such as: the targets' dimension/shape, the radar wavelength and its angle of incidence. Due to this complexity, it is very difficult to estimate a correct value for it. However, by choosing a metal object with the correct shape and positioning, the RCS can be increased by several tens of dB. Nonetheless, the model presented in this section represents the best estimation within this framework.

Finally, from the receiver side, the RF signal is down-converted to the IF frequency (with an associated gain of 4dB) and then is amplified before passing through the optical link. Since the IF signal power is low, there is no risk of saturation in neither the amplifier at the point I and the optical link, thus the amplifier board with 3 amplifier stages can also be used at the receiver side (figure 4.22a). Following the same approach as with the transmitter side, the signal power budget estimation across the receiver side is depicted in table 4.6 :

	Power at Point K	**Rx Amplifier Gain**	**Power at Point L**	**Optical Link Losses**	**Power at Point M**
IF signal (Best Case)	-68dBm	55dB	-13dBm	31.6dB	-44.6dBm
IF signal (Worst Case)	-74dBm	55dB	-19dBm	31.6dB	-50.6dBm

Table 4.6: Signal power - receiver side

From table 4.6 we see that at the USRP Rx channels the received IF signal power is estimated to be between -50.6dBm and -44.6dBm, which is within the USRP supported power interval (-65dBm to -15dBm).

In conclusion, this analysis represents a preliminary estimation of how the system is predicted to behave, based on its own architecture and scenario simulation. The estimations also take into account the characteristics of each module integrated in the setup.

4.10 Experimental Results

After doing the integration of the whole system and doing performance estimations based on the characteristics of each module, in this section, experimental results are presented and analysed by considering the system as a whole.

To achieve the experimental results, the setup depicted in figure 4.30 was mounted (following the decisions made in section 4.9). This setup shows laboratory equipment that replaces the USRP, Reference generator and the PLL, seen in figure 4.29, that due to some constraints beyond this framework, were not used. As figure 4.30 depicts, an Arbitrary Waveform Generator (AWG) and a Vector Signal Generator (PSG) are used to generate the OFDM signal at the IF frequency. Also, two signal generators are used to substitute the reference generator and the PLL. Finally, this setup comprises a Vector Signal Analyzer (VSA), whose function is to check the signals at several testing points.

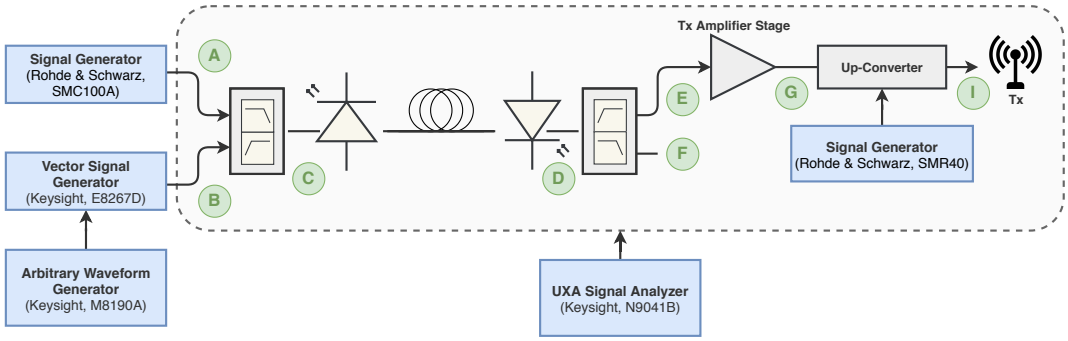

Figure 4.30: Experimental setup

Firstly, the signals needed to test the setup must be generated. For the 10MHz reference signal, the SMC100A signal generator is used, and its output is depicted in figure 4.31a. The 100MHz-OFDM waveform with QPSK modulation was based on a 5G signal that was generated using the Keysight's *Signal Studio Pro*, being subsequently loaded into the AWG. The AWG's output is connected to the PSG's input where the OFDM signal is up-converted to the IF frequency (3.84GHz), as figure 4.31b demonstrates:

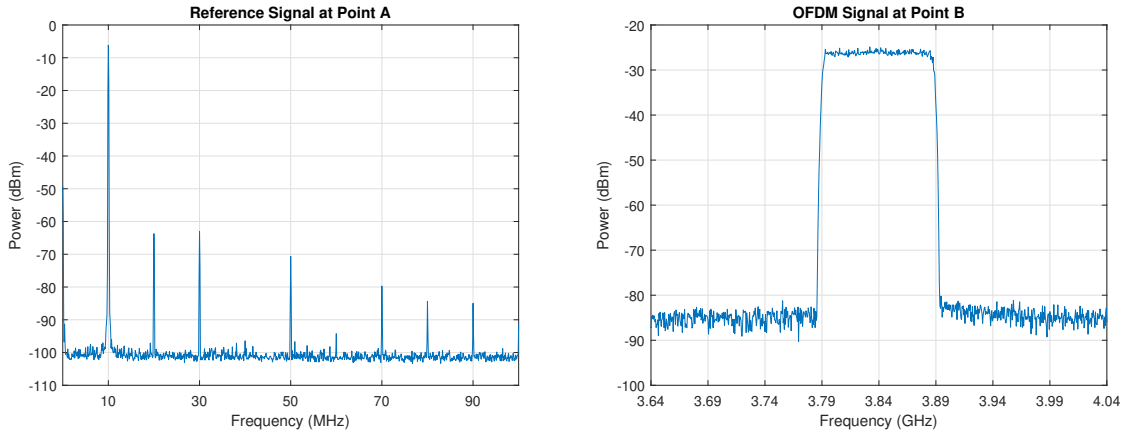

(a) Generated reference signal

(b) Generated OFDM signal

Figure 4.31

By evaluating figure 4.31 we see that both the reference and OFDM signals were well generated. Regarding the 10MHz reference signal, it has an approximate power of -6.6dBm (following the estimations of section 4.9) and we can also see some negligible side lobes. By integrating the OFDM signal power (visible in figure 4.31b) over its bandwidth we get -11.3dBm/100MHz, following the suggested power in section 4.9.

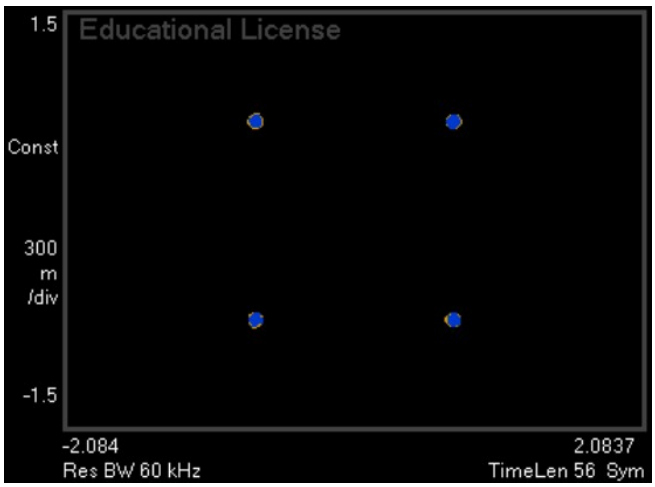

Figure 4.32: Constellation at point B

The constellation depicted in figure 4.32 represents the demodulated OFDM signal that is transmitted at point B. This representation is very important to understand the distortions introduced by the setup throughout its different stages. In this case the signal is transmitted with great quality as the constellation points are practically at the ideal positions (according to the QPSK modulation) since the Error Vector Magnitude (EVM), which represents how deviated the constellation points are from their ideal positioning, has an approximate value of 1.5 %

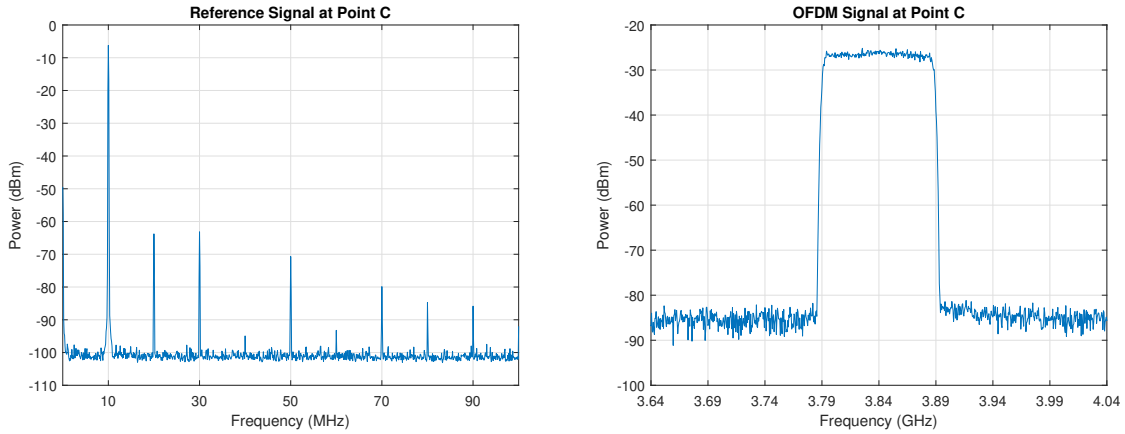

(a) (b)

Figure 4.33: Reference and OFDM signals at point C

From figure 4.33 we see that the diplexer introduces some minor losses ($< 1dB$) in each signal, as estimated.

Between point C and point D is one of the critical sections of the setup. According to optical link characterization in section 4.4 and the estimations performed in section 4.9, it is expected for the optical link to introduce approximately 16.5dB and 28.5dB of attenuation for the reference and OFDM signals, respectively (disregarding the optical mux/demux).

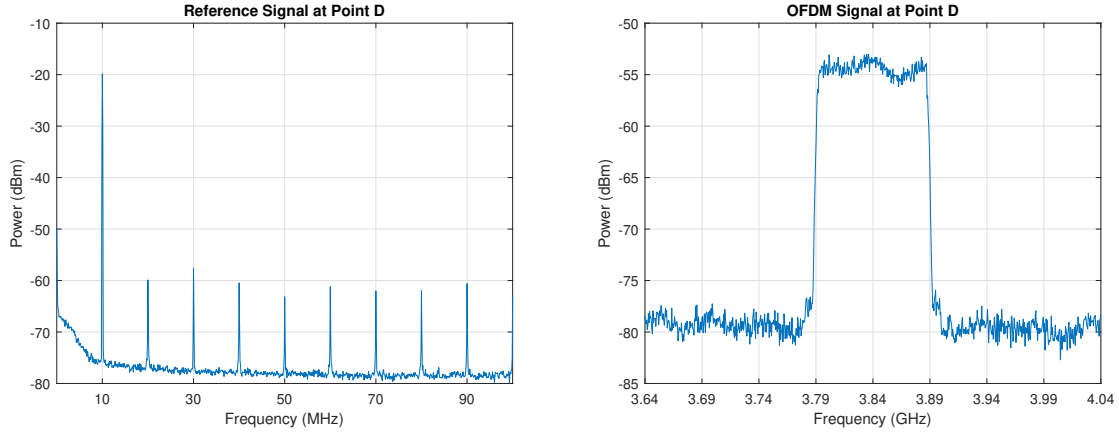

(a) (b)

Figure 4.34: Reference and OFDM signals at point D

From figure 4.34a we see that the reference signal has approximately -24dBm of power, which corresponds to an attenuation of 17.4dB in relation to its power at point C. Turning now to figure 4.34b, by integrating the signal power over its bandwidth, we get -39.6dBm/100MHz of average power, which corresponds to an attenuation of approximately 28dB in relation to point C.

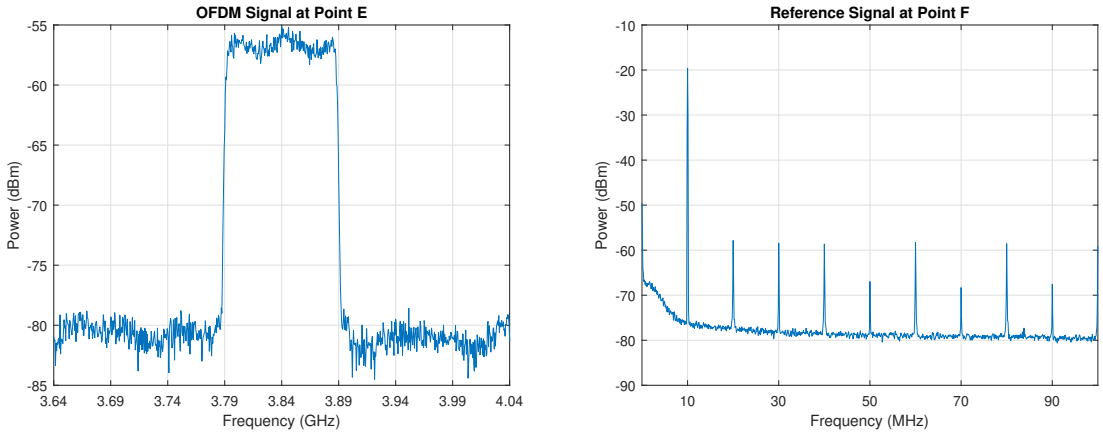

(a) (b)

Figure 4.35: OFDM and reference signals at points E and F, respectively

As with the first diplexer, the one at point D does not introduce major attenuation or distortions to the signals, as figure 4.35 demonstrates.

Since the optical link is a critical point, it is of great interest to analyse the distortions of the signal after it passes through it. In this context, figure 4.36 shows us that the constellation points of the signal at point E have some error ($EVM \approx 10\%$) that, in comparison with the transmitted signal (4.32), indicates some distortion introduced by the optical link. However, the constellation points are perfectly distinguishable, demonstrating a good performance of the link. As a side note, the two different color dots that can be seen in figure 4.36, are related to the 5G standard, that sends some control subcarriers (pilots) in a specific part of the signal bandwidth (in blue) alongside with data (in brown).

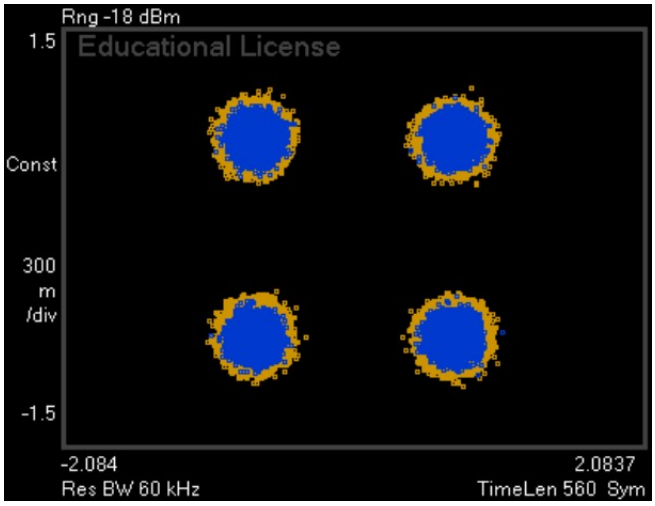

Figure 4.36: Constellation at point E

Another important section of the setup that is within this framework, is the amplifier module. From its characterization in section 4.5 and the estimations made in section 4.9, the amplifier module is supposed to have a gain of 55dB. By integrating the OFDM signal power

over its bandwidth we get 3dBm of average power at point G, which translates into a gain of 42.6dB between points E and G (for the case with no attenuation added at the amplifier). The signal in figure 4.37b is the OFDM signal at point G when the attenuator before the last amplifier stage is programmed with 15dB of attenuation. This signal has -4.8dBm of average power, which means that in comparison with the signal before the amplifier (figure 4.35a) it has a gain of approximately 50 dB.

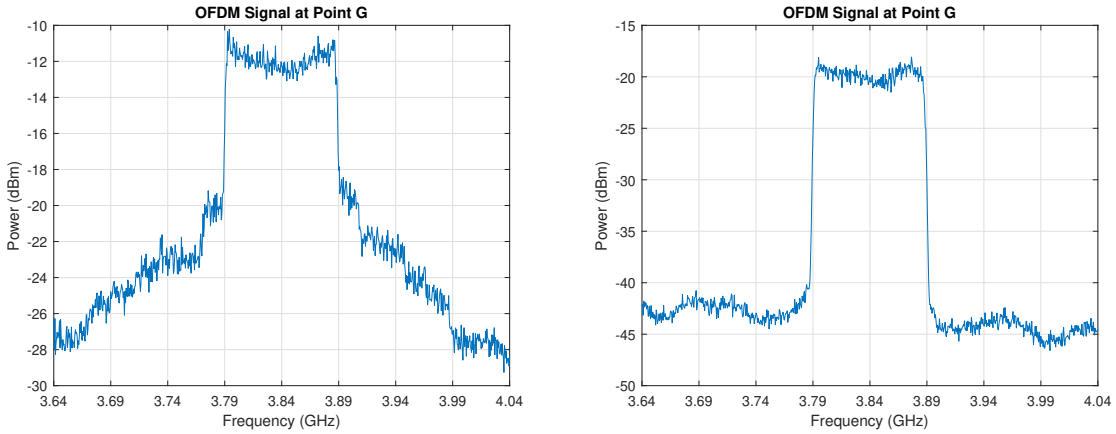

(a) OFDM signal at point G : 0dB Att

(b) OFDM signal at point G : 15dB Att

Figure 4.37: OFDM signal at points G

Furthermore, by analysing the constellations for each of the scenarios, it is clear that when the attenuation is set to 0dB ($(EVM \approx 16\%)$, the signal gets a larger distortion when compared to the one with the attenuation set to 15dB ($EVM \approx 10\%$). Thus it is possible to conclude that the signal in figure 4.37a is starting to saturate at the third amplifier stage whereas the one in figure 4.37b is not.

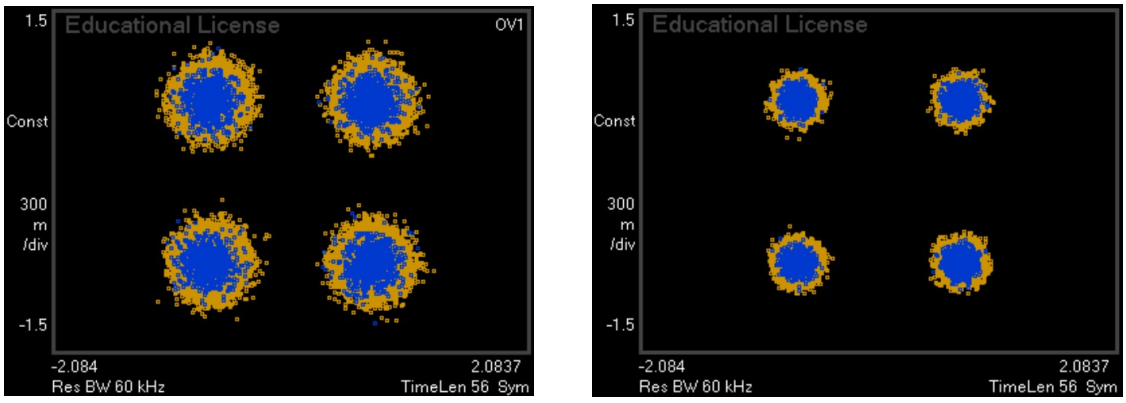

(a) Constellation at point G : 0dB Att

(b) Constellation at point G : 15dB Att

Figure 4.38: Constellation at point G

Having the saturation problem in mind, the 15dB attenuated signal was the one to feed the up-converter:

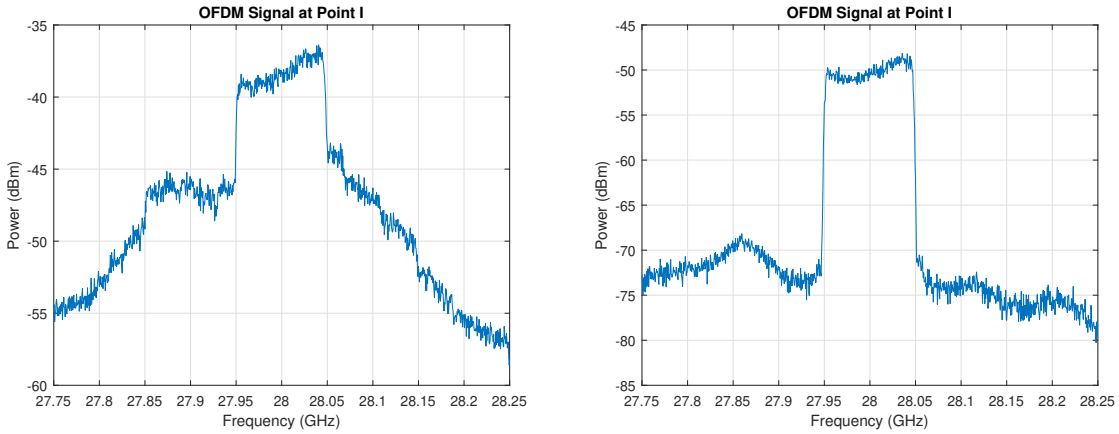

(a) OFDM signal at point I : 15dB Att (b) OFDM signal at point I : 31.5dB Att

Figure 4.39: OFDM signal at points I

The 28GHz up-converted OFDM signal (figure 4.39a) has an average power of -23.3dBm which represents an attenuation of 18.5dB in relation to the signal at point G (figure 4.37b). As detailed in table 4.3, the up-converter module is expected to attenuate the signal by 1dB only, instead of the observed 4.5dB. In order to overcome this problem, and to dismiss some saturation that might be happening, the attenuation a the third amplifier stage was set to its maximum (31.5dB) and the correspondent signal at the output of the up-converter was measured (as seen in figure 4.39b).

By looking at the correspondent constellation maps of figure 4.40 we see that, for both scenarios, the signal has some extra distortion, having the one at figure 4.40a an EVM of $\approx 14\%$ and the one at figure 4.40b an EVM of $\approx 12\%$. Thus, we can conclude that, for an attenuation of 15dB at the third amplifier stage, the up-converter starts to saturate.

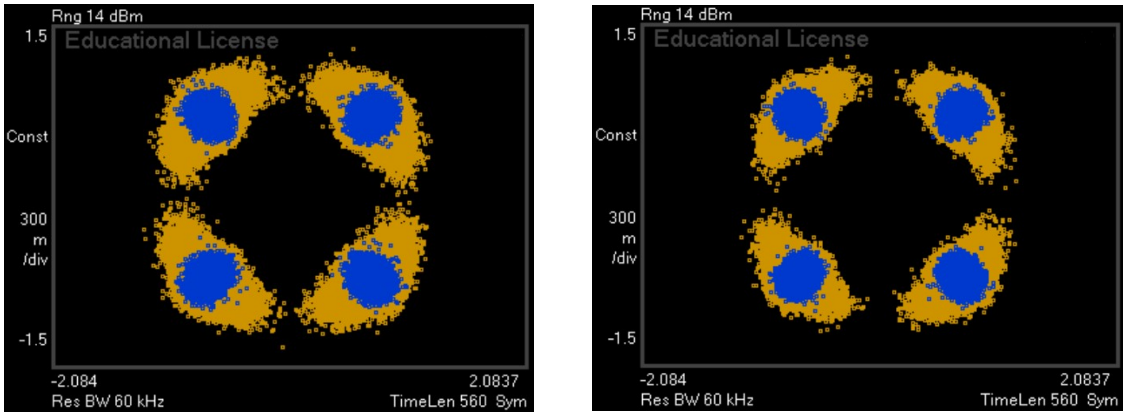

(a) Constellation at point I : 15dB Att (b) Constellation at point I : 31.5dB Att

Figure 4.40: Constellation at point I

Another curious thing these results show is that the pilot subcarriers (that occupy a specific bandwidth section and are represented in blue) have a low error. This indicates some problem that the up-converter might have, regarding the mixing process, that is heavily

distorting some of the signal's subcarriers, as the great dispersion of data constellation points (in brown) demonstrates.

To investigate this problem, the same measurements were made, but the IF frequency and the LO frequency were changed to 2GHz and 11GHz, respectively. According to expression 4.2, the frequency of the new up-converted signal is 24GHz and the resulting constellation is depicted in figure 4.41:

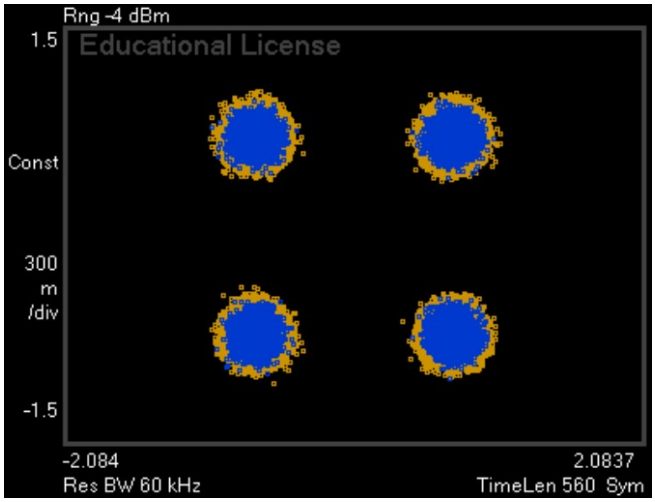

Figure 4.41: Constellation at point I with parameter adjustments

This constellation shows a clear improvement in relation to the ones in figure 4.40 by having an EVM of 10 %, approximately. Furthermore, it confirms that the up-converter performance is dependent to the mixer's product.

CHAPTER 5

Conclusions and Future Work

5.1 Summary and Conclusions

The number of use cases in which the Radar technology becomes attractive is increasing exponentially as the world is evolving into a data-oriented society, where advanced detection and communication systems are needed to connect a wide spectrum of new smart devices. In this dissertation, a new Radar technology with potential to jointly integrate detection and communication systems were presented, as well as engineered a preliminary setup that embraces the *Photonics-Based Widely Distributed MIMO Radar* technology.

After presenting a brief history of Radar, this dissertation discusses two Radar waveforms along with a theoretical explanation of how to correctly detect a target's position and velocity. The first waveform explored is FMCW, however, it was chosen to proceed with the OFDM waveform because of its potential for communication systems. Next to comparing the classical monostatic Radar approach with the new *Widely Distributed* one, a simulator was build and simulation results were presented. The simulator and its results were very important for this work because they had to be achieved in agreement with the setup development. There were several simulation iterations in order to find a configuration with good results so that they could be transposed to the experimental setup.

The engineering of the preliminary setup was also a challenge, because not only it had to match the simulation, but a correct understanding of all the setup modules was needed so the specific ones built in this framework (namely, the optical link and the amplifier stages) would match the already developed modules. Regarding the development of the amplifier modules, some precautions were taken for debugging purposes to ensure that if any board failed, the problem could be easily detected. Due to the precautions taken during the development phase, the boards worked as expected, without any problem. Regarding the optical link, some limitations were found: first, it was concluded that the laser has a poor E/O conversion, introducing a frequency dependent attenuation; second, it was experimentally verified that the photodetector has a TIA that gets easily saturated. In order to keep the setup as simple and cheap as possible, these limitations had to be tackled, and to do so, a full setup analysis was carried out, during which several problems were identified and corrected to ensure that the configuration is suitable for practical tests of the Radar system. Finally, preliminary experimental testing was made. To achieve the first experimental results, the setup had

to be adjusted since some modules that were out of the scope of this framework were not completely characterized. Yet, promising results were accomplished since they were according the estimations, which indicates a good characterization of the transmission system.

In conclusion, the main objectives of this dissertation were achieved. For the simulation part, several MIMO algorithms and Radar waveforms were studied and evaluated. Important factors such as the number of antennas and its spatial distribution were taken into account in order to develop a *Widely Distributed MIMO* simulator capable of testing different setup scenarios. For the hardware and implementation part, three amplifier boards were successfully developed and tested. Also, the optical link characterization was correctly done and enabled the understanding of its limitations. Furthermore, all the system modules were characterized and integrated to achieve a workable setup. With regard to the experimental testing, preliminary results were achieved, however, mainly due to time constraints and also due to the difficulty in integrating the USRP module into the setup, the performance of the Radar functionality was not evaluated.

5.2 Future Work and Recommendations

As exposed along this dissertation, there are some limitations that can be exceeded in a future work as well as some results that must be obtained in order to improve the setup performance. So, from the experience acquired along this work, the following future work and recommendations are proposed:

- The simulator considers a perfect environment with isotropic antennas, simple targets and no path losses and these are not real life conditions, so a good future task would be to improve the models used in the simulator in order to improve the agreement between simulation and reality.
- In terms of the hardware, the first thing to do should be completing the preliminary tests with a single target and evaluate some setup adjustments to achieve a fully functioning link.
- After testing with a target, it is suggested to start looking for improvements: either software or hardware. For the results obtained within this framework, a good improvement would be changing the IF from 3.84GHz to a lower frequency, where the optical link would have minor losses and the amplifiers would perform better. However, these changes should be synchronous with the rest of the participants of the RETIOT project.
- In a more advanced phase, the fusion of the Radar and communication functionalities would be of interest, using the OFDM waveform as the key to achieve a joint communication and detection system, opening several new use cases.

References

[1] T. Kawanishi, T. Miura, and K. Inagaki. Reconfigurable radio-over-fibre networks for interference mitigation in linear cell radars. In *2019 21st International Conference on Transparent Optical Networks (ICTON)*, pages 1–3, 2019.

[2] M. I. Skolnik. *Introduction to Radar Systems /2nd Edition.* McGraw Hill Book Co., New York, 2 edition, 1980.

[3] R V Jones. Radar days. *Physics Bulletin*, 38(12), dec 1987.

[4] V.S. Chernyak. Fundamentals of multisite radar systems. *New York: Gordon and Breach*, 1998.

[5] A. M. Haimovich, R. S. Blum, and L. J. Cimini. Mimo radar with widely separated antennas. *IEEE Signal Processing Magazine*, 25(1):116–129, 2008.

[6] P. Ghelfi, L. Lembo, F. Scotti, G. Serafino, S. Maresca, and A. Bogoni. Distributed coherent radars enabled by fiber networks. In *2019 21st International Conference on Transparent Optical Networks (ICTON)*, pages 1–4, 2019.

[7] E. Fishler, A. Haimovich, R. S. Blum, L. J. Cimini, D. Chizhik, and R. A. Valenzuela. Spatial diversity in radars—models and detection performance. *IEEE Transactions on Signal Processing*, 54(3):823–838, 2006.

[8] D. W. Bliss and K. W. Forsythe. Multiple-input multiple-output (mimo) radar and imaging: degrees of freedom and resolution. In *The Thrity-Seventh Asilomar Conference on Signals, Systems Computers, 2003*, volume 1, pages 54–59 Vol.1, 2003.

[9] P. Ghelfi, F. Laghezza, F. Scotti, G. Serafino, A. Capria, S. Pinna, D. Onori, C. Porzi, M. Scaffardi, A. Malacarne, V. Vercesi, E. Lazzeri, F. Berizzi, and A. Bogoni. A fully photonics-based coherent radar system. *Nature*, 507:341–345, 2014.

[10] F. Laghezza, F. Scotti, G. Serafino, L. Banchi, V. Malaspina, P. Ghelfi, and A. Bogoni. Field evaluation of a photonics-based radar system in a maritime environment compared to a reference commercial sensor. *IET Radar, Sonar Navigation*, 9(8):1040–1046, 2015.

[11] L. Lembo, P. Ghelfi, and A. Bogoni. Analysis of a coherent distributed mimo photonics-based radar network. In *2018 15th European Radar Conference (EuRAD)*, pages 170–173, 2018.

[12] Rajbir Singh, Manoj Ahlawat, and Deepak Sharma. A review on radio over fiber communication system. 6:2319–7471, 04 2017.

[13] N. H. Lehmann, A. M. Haimovich, R. S. Blum, and L. Cimini. High resolution capabilities of mimo radar. In *2006 Fortieth Asilomar Conference on Signals, Systems and Computers*, pages 25–30, 2006.

[14] S. M. Patole, M. Torlak, D. Wang, and M. Ali. Automotive radars: A review of signal processing techniques. *IEEE Signal Processing Magazine*, 34(2):22–35, 2017.

[15] Belinda J. Lipa and Donald E. Barrick. Fmcw signal processing. *Mirage Systems, Sunnyvale, California*.

[16] Suleyman Suleymanov. Design and implementation of an fmcw radar signal processing module for automotive applications. *MSc Dissertation, University of Twente*, 2016.

[17] Atílio Gameiro, Daniel Castanheira, Jessica Sanson, and Paulo Monteiro. Research challenges, trends and applications for future joint radar communications systems. *Wireless Personal Communications*, 100, 03 2018.

[18] I. Orović, N. Žarić, S. Stanković, I. Radusinović, and Z. Veljović. Analysis of power consumption in ofdm systems. In *2011 Proceedings of the 34th International Convention MIPRO*, pages 653–657, 2011.

[19] I. Baig and V. Jeoti. Papr reduction in ofdm systems: Zadoff-chu matrix transform based pre/post-coding techniques. In *2010 2nd International Conference on Computational Intelligence, Communication Systems and Networks*, pages 373–377, 2010.

[20] Rajiv Ramaswami, Kumar Sivarajan, and Galen Sasaki. *Optical Networks: A Practical Perspective, 3rd Edition - Chapter 2*. Morgan Kaufmann Publishers Inc., San Francisco, CA, USA, 3rd edition, 2009.

[21] Nathan J. Gomes ; Paulo P. Monteiro ; Atílio Gameiro. Next generation wireless communications using radio over fiber. *IEEE Signal Processing Magazine*, page Chapter 4, 2012.

[22] Marco Fernandes. Digital pre-distortion for 5g transmission over high-capacity optical fronthaul fiber links. *MSc Dissertation*, University of Aveiro, 2019.

[23] Bruno Brandão. Development of a remote radio unit and optical access link for the orcip c-ran testbed. *MSc Dissertation*, University of Aveiro, 2019.

[24] S. Saseendran, K. Bhowmick, and T. Sreenivasulu. Design of photonic crystal based demultiplexer for cwdm technology. In *2017 IEEE International Conference on Advanced Networks and Telecommunications Systems (ANTS)*, pages 1–4, 2017.

[25] R. Arruela, D. MARINHO, T. Varum, and J. M. Matos. A ka-band frontend for mmwave mimo and beamforming applications. In *International Microwave and Optoelectronics Conf. - IMOC*, pages –, November 2019.

[26] Mark A Richards. Fundamentals of radar signal processing. *Tata McGraw-Hill Education*, 2005.

APPENDIX A

OFDM MIMO Radar with Widely Seperated Antennas - Simulation Code

OFDM MIMO Radar with Widely Separated Antennas

The following code is based on:

A. M. Haimovich, R. S. Blum and L. J. Cimini, "MIMO Radar with Widely Separated Antennas," in *IEEE Signal Processing Magazine*, vol. 25, no. 1, pp. 116-129, 2008.

L. Lembo, P. Ghelfi and A. Bogoni, "Analysis of a Coherent Distributed MIMO Photonics-Based Radar Network," *2018 15th European Radar Conference (EuRAD)*, Madrid, 2018, pp. 170-173.

System Parameters

Work Enviroment Clearence:

```
close all
clear all
```

Physical Constants

```
c0 = 299792458;       % Speed of light
SNR = 30;             % Signal to noise ratio (dB)
```

OFDM Parameters

```
OFDM.B = 100e6;                         % OFDM symbol bandwidth
OFDM.N = 8;                             % Number of Subcarriers
OFDM.fc = 28e9;                         % Carrier frequency
OFDM.df = OFDM.B/OFDM.N;                % Carrier frequency spacing
M = 4;                                  % Modulation order
num_PSKsymb = 8;                        % Number of QPSK symbols
data = randi([0 M-1],num_PSKsymb,1);
OFDM.symb = pskmod(data,M);
```

Radar Resolution

```
radar.rangeResolution.noncoherent = c0/(2*OFDM.B);   % Resolution non-coherent
radar.rangeResolution.coherent = c0/OFDM.fc;         % Resolution coherent
radar.unambiguousRange = OFDM.N*c0/(2*OFDM.B);       % Unambiguous range
```

Radar Image Properties

Two methods may be used to compute the radar image, non-coherent and coherent methods. The first yields worse resolution, inversely proportional to the signal bandwidth, and the second better resolution, on the order of the wavelength. However, the last requires time and phase synchronization and the first only time synchronization.

```
radarImage.axis = [-10, 10, -8, 8]; % Limits radar image [xmin, xmax, ymin, ymax] (m)
radarImage.width = 128; radarImage.height = 128;
```

Define Antenna/ Target Positions

```
scenario = ScenarioParameters();
```

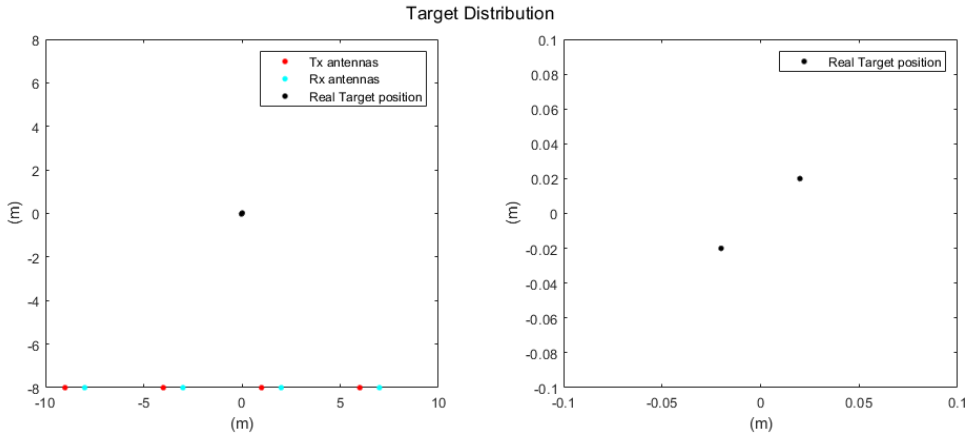

Get received signal

Obtain the received signal using the *OFDM* parameters previously defined and add noise.

```
Z = getReceivedSignal(scenario, SNR, OFDM, c0);
```

Signal Processing

Non-Coherent method

Select the signal processing method.

```
radarImage.method = 'non-coherent';
```

Compute radar image, for all possible positions pairs $[x, y]$ compute the log-likelihood.

```
[x_axis, y_axis, data] = computeRadarImage(radarImage, scenario, OFDM, Z, c0);
```

Plot results.

```
figure;
displayRadarImage(x_axis, y_axis, data, scenario);
title('Non-coherent method: Spectrum')
```

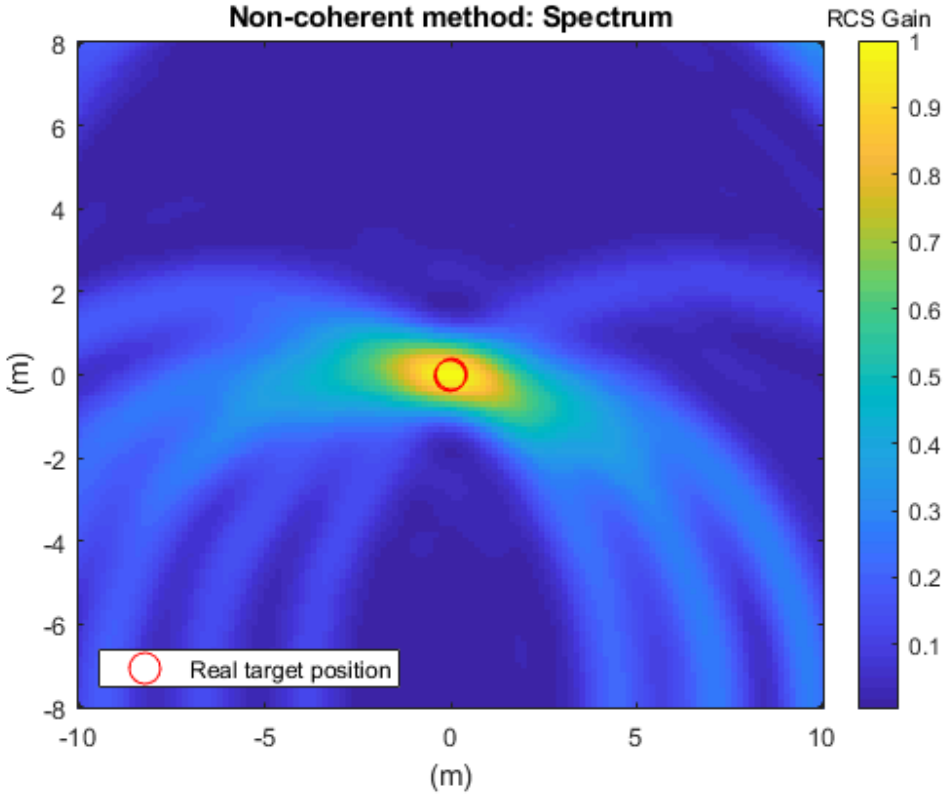

Coherent method

For the coherent method the resolution is $f_c/(2B)$ times higher than the non-coherent method. Therefore, for the radar image processing, the limits are reduced considerably for the computation duration to be similar to the non-coherent method.

```
radarImage.method = 'coherent';
radarImage.axis = [-0.1, 0.1, -0.1 0.1];
```

Compute radar image, for all possible positions pairs $[x, y]$ compute the log-likelihood.

```
[x_axis, y_axis, data] = computeRadarImage(radarImage, scenario, OFDM, Z, c0);
```

Plot results.

```
figure;
displayRadarImage(x_axis, y_axis, data, scenario);
title('Coherent method: Spectrum')
```

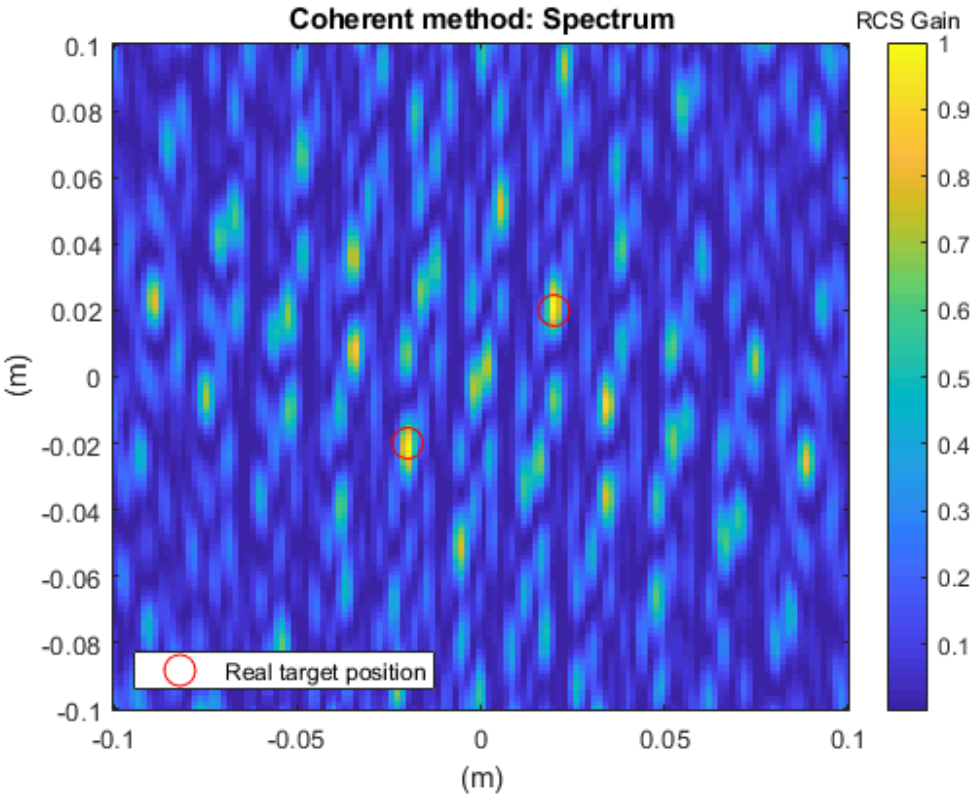

Ambiguity Functions Calculation

Scenario Adjustment

Now, a single target at the origin is considered.

```
scenario=targetOrigin(scenario)
```

```
scenario = struct with fields:
         tx: [1×1 struct]
         rx: [1×1 struct]
    targets: [1×1 struct]
```

```
Z = getReceivedSignal(scenario, SNR, OFDM, c0);
```

Non-Coherent Ambiguity Function

Ambiguity function for the non-coherent method is calculated.

```
radarImage.method = 'non-coherent';
radarImage.axis = [-10, 10, -8, 8];
[x_axis, y_axis, data] = computeRadarImage(radarImage, scenario, OFDM, Z, c0);
displayAmbiguityFunction(radarImage,data)
```

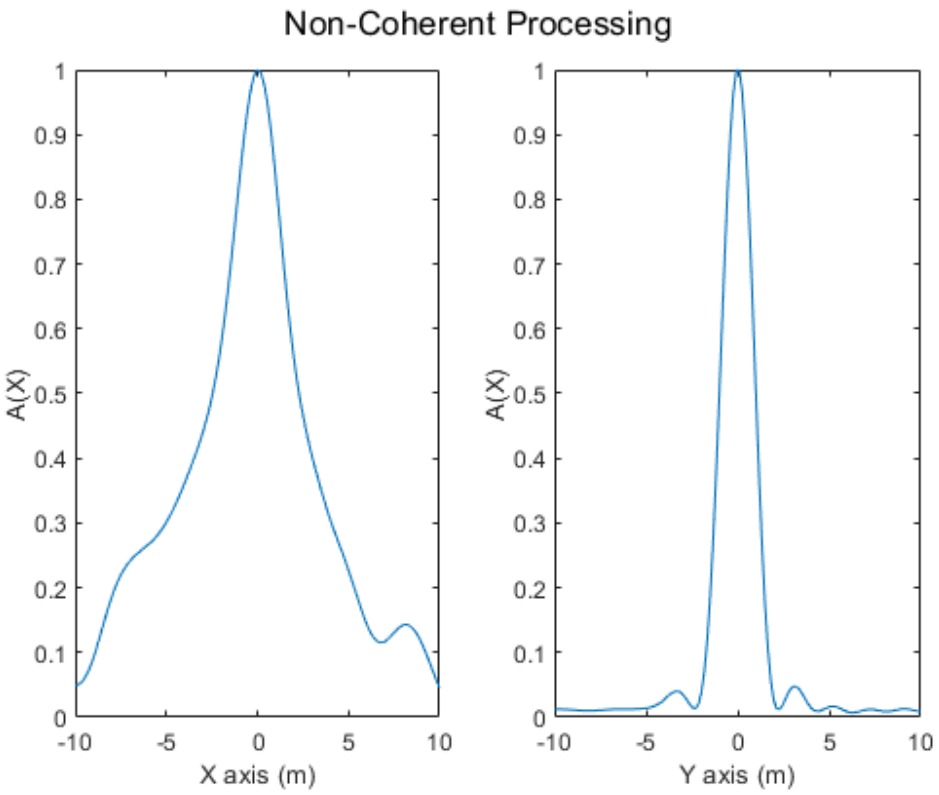

Coherent Ambiguity Function

Ambiguity function for the non-coherent method is calculated:

```
radarImage.method = 'coherent';
radarImage.axis = [-0.1, 0.1, -0.1 0.1];
[x_axis, y_axis, data] = computeRadarImage(radarImage, scenario, OFDM, Z, c0);
displayAmbiguityFunction(radarImage,data)
```

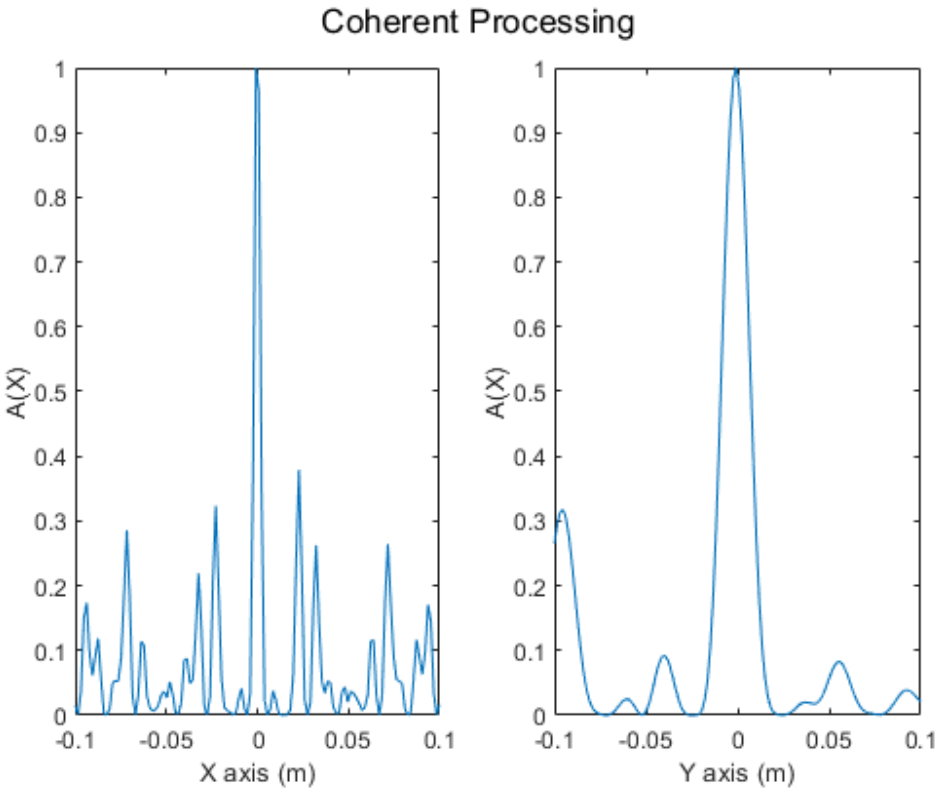

FUNCTIONS

Get Received Signal

Taking into consideration a given *scenario* and *SNR* this function generates an *OFDM* for each transmit antenna and adds noise to the received signal of each receiver.

```
function Z = getReceivedSignal(scenario, SNR, OFDM, c0)
% The transmitted signal is a OFDM with N samples, bandwidth B and ramp time Tu
[x, t] = generateWaveform(OFDM);

% which is upconverted to the carrier frequency fc
xup = upconvert(x, OFDM.fc, t);

% The received signal at antenna l due to the
% transmission from antenna m is the superposition of Q delayed copies of the tx signal,
% reflected by the targets
Zup = getRxSignal(OFDM, scenario, c0);

% After the downconversion the received signal is
Z = downconvert(Zup, OFDM.fc, t);
```

```
% Adding  noise
Z = addNoise(Z, SNR);
end
```

Generate waveform

Generate N samples of OFDM signal time shifted by t_d seconds, with bandwidth B.

The function outputs the OFDM signal x and the time t.

```
function [x, t] = generateWaveform(OFDM, td)

% If not specified the considered time delay is set to zero
if(nargin == 1); td = 0; end

% OFDM parameters
OFDM.Tsymb = OFDM.N/OFDM.B;
Ts= 1/OFDM.B;
% Sampling time
n= (0:OFDM.N-1);
t= (0:OFDM.N-1)'*Ts;

% Signal generation
x = ifft(OFDM.symb.*exp(-1j.*2.*pi.*n.*OFDM.df.*td)');
end
```

Upconvert signal

Upconvert signal x to carrier frequency f_c.

```
function xup = upconvert(x, fc, t)
xup = exp(1j*2*pi*fc*t).*x;
end
```

Downconvert signal

Downconvert signal x from carrier frequency f_c.

```
function x = downconvert(xup, fc, t)
x = exp(-1j*2*pi*fc*t).*xup;
end
```

Compute distance

Compute distance from point r to q plus distance from point p to t.

```
function d = computeDistance(r, p, t)
d = norm(r - p) + norm(p - t);
end
```

Compute received signal

The received signal at antenna l due to the transmission from antenna m is the superposition of Q delayed copies of the Tx signal, reflected by the targets.

```
function Z = getRxSignal(OFDM, scenario, c0)
% Pre-allocate memory
Z = zeros(OFDM.N, scenario.rx.nrAntennas, scenario.tx.nrAntennas);
% Z(:, l, k): received signal at antenna l from antenna k

% Compute all delays for the considered scenario
td = computeDelays(scenario, c0);

% For each tx rx pair compute the rx signal as a superposition of the Q delayed components
for idx = 1:scenario.rx.nrAntennas*scenario.tx.nrAntennas
    % Converts the single index 'idx' to two indexes l,m
    [l, m] = ind2sub([scenario.rx.nrAntennas, scenario.tx.nrAntennas], idx);
    for q = 1:scenario.targets.nr
        % Superimpose the qth target delayed signal scaled by gain g
        % Synthetise delayed tx signal at baseband
        [x, t] = generateWaveform(OFDM, td(q, l, m));
        xup = upconvert(x, OFDM.fc, t - td(q, l, m)); % Upconvert to carrier fc
        g = scenario.targets.gain.magnitude(q)*scenario.targets.gain.phase(q);
        Z(:, l, m) = Z(:, l, m) + g*xup;              % Scale by gain g of target q and superi
    end
end
end
```

Add noise to signal

This functions adds noise to signal X, considering a signal to noise ratio (SNR) equal to SNR.

```
function Y = addNoise(X, SNR)
noise = 10^(-SNR/20)*complex(randn(size(X)), randn(size(X)))/sqrt(2);
Y = X + noise;
end
```

Compute AntennasDelays

```
function D = computeDelays(scenario, c0)
% Pre-allocate memory
D = zeros(scenario.targets.nr, scenario.rx.nrAntennas, scenario.tx.nrAntennas);

% For all targets
for q = 1:scenario.targets.nr
    % For all rx antennas
    for l = 1:scenario.rx.nrAntennas
        % For all tx antennas
        for m = 1:scenario.tx.nrAntennas
            % compute delay
            D(q, l, m) = 1/c0*computeDistance(scenario.rx.positions(l, :),...
```

```
                scenario.targets.positions(q, :), scenario.tx.positions(m, :));
        end
    end
end
end
```

Compute radar image

Compute radar image for the considered scenario using the received signal Z and the properties of the transmitted OFDM signal.

Two methods may be considered for the computation, 1) non-coherent processing, 2) coherent processing.

```
function [x_axis, y_axis, data] = computeRadarImage(radarImage, scenario, OFDM, Z, c0)
    % Select the processing function accordingly to the method
    switch radarImage.method
        case 'non-coherent'
            pfunc = @(x) abs(x)^2;   % The abs removes the phase p
        case 'coherent'
            pfunc = @(x) x;
    end

    % x and y axis points
    x_axis = linspace(radarImage.axis(1), radarImage.axis(2), radarImage.width);
    y_axis = linspace(radarImage.axis(3), radarImage.axis(4), radarImage.height);
    p
    % re-allocate memory
    data = zeros(radarImage.width, radarImage.height);

    for x_idx = 1:length(x_axis)
        for y_idx = 1:length(y_axis)
            testPoint = [x_axis(x_idx), y_axis(y_idx)];
            for l = 1:scenario.rx.nrAntennas
                for m = 1:scenario.tx.nrAntennas
                    td = 1/c0*computeDistance(scenario.rx.positions(l, :),...
                        testPoint, scenario.tx.positions(m, :));

                    % Synthetise delayed tx signal at baseband
                    %(which corresponds to delay for each point in xy plan)
                    x = generateWaveform(OFDM, td);
                    p = exp(-1j*2*pi*OFDM.fc*td);   % Phase rotation due to carrier fc
                    xup = p*x;                      % Delayed tx signal with phase rotation
                    data(x_idx, y_idx) = data(x_idx, y_idx) + pfunc(xup'*Z(:, l, m));

                end
            end
        end
    end

    % Return the abs value
    switch radarImage.method
        case 'non-coherent'
            data = abs(data)';
```

```
            % The transpose is used to plot the image correctly with the imagesc function
        case 'coherent'
            data = abs(data)'.^2;
    end
end
```

Display Radar Image

Plotting of the non-coherent/coherent radar images.

```
function [] = displayRadarImage(x_axis, y_axis, data, scenario)
    % Plot radar image
    imagesc(x_axis, y_axis, data/max(max((data)))); hold on
    cb=colorbar;
    set(get(cb,'Title'),'String','RCS Gain');

    set(gca,'YDir','normal'); % Set axis to normal, since imagesc reverses the Y axis

    % Plot real positions of the targets
    plot(scenario.targets.positions(:, 1), scenario.targets.positions(:, 2), 'ro',...
        'markerSize', 12);
    hold off
    xlabel('(m)');
    ylabel('(m)');
    legend('Real target position', 'location', 'southwest');
end
```

Scenario Parameters

Definition of the number of antennas and type of placement (random, optimal or manual).

```
function [scenario] =ScenarioParameters()
    best_var = input('Best config? y/n [Y]: ','s');
    if isempty(best_var)
        best_var = 'Y';
    end
    if (best_var == 'y' || best_var == 'Y')
        scenario.tx.nrAntennas =4;
        scenario.rx.nrAntennas =4;
        scenario.tx.positions = [-9,-8;-4,-8;1,-8;6,-8];
        scenario.rx.positions = [-8,-8;-3,-8;2,-8;7,-8];
    else
        scenario.tx.nrAntennas =input('Choose Number of TX antennas: ');
        scenario.rx.nrAntennas =input('Choose Number of RX antennas: ');
        disp('-----------------------------------------------');
        rand_var = input('Random? y/n [Y]: ','s');
        if isempty(rand_var)
            rand_var = 'Y';
        end
        if ( rand_var == 'y' || rand_var == 'Y')
            scenario.tx.positions =... % Random uniform position between -10 and 10
```

```
                10*(rand(scenario.tx.nrAntennas, 2) - 1/2);
            scenario.rx.positions =... % Random uniform position between -10 and 10
                10*(rand(scenario.rx.nrAntennas, 2) - 1/2);
        else
            scenario.tx.positions=zeros(scenario.tx.nrAntennas,2);
            for i=1:scenario.tx.nrAntennas
                disp(' ');
                disp(['TX antenna(',num2str(i),')']);
                scenario.tx.positions(i,1)=input('X Coordinate(-10,10):' );
                scenario.tx.positions(i,2)=input('Y Coordinate(-8,8):' );
            end
            disp('-----------------------------------------------');
            scenario.rx.positions=zeros(scenario.rx.nrAntennas,2);
            for i=1:scenario.rx.nrAntennas
                disp(' ');
                disp(['RX antenna(',num2str(i),')']);
                scenario.rx.positions(i,1)=input('X Coordinate(-10,10):' );
                scenario.rx.positions(i,2)=input('Y Coordinate(-8,8):' );
            end
            disp('-----------------------------------------------');
        end
    end
```

Definition of the number and positioning of the targets.

```
    % Target Parameters
    scenario.targets.nr=input('Choose Number of Targets: ');
    scenario.targets.matrix=zeros(scenario.targets.nr,2);

    for i=1:scenario.targets.nr
        scenario.targets.matrix(i,1)=input('X Coordinate(-10,10):' );
        scenario.targets.matrix(i,2)=input('Y Coordinate(-8,8):' );
    end
    scenario.targets.positions = scenario.targets.matrix;% [x-axis, y-axis] Position (m)
    displaySpaceInfo(scenario)

    scenario.targets.gain.magnitude =...    % All targets have unitary gain
        rand(scenario.targets.nr, 1)*0+1;
    scenario.targets.gain.phase = ...       % Unitary phase shift for each target
        exp(1j*2*pi*rand(scenario.targets.nr, 1))*0+1;

end
```

Set target to Origin

Redefine of the *scenario.target* to be a single target at origin.

```
function [scenario] = targetOrigin(scenario)
    scenario.targets.nr=1;
    scenario.targets.matrix=zeros(1,2);
    scenario.targets.gain.magnitude = rand(scenario.targets.nr, 1)*0+1;
    scenario.targets.gain.phase = exp(1j*2*pi*rand(scenario.targets.nr, 1))*0+1;
```

```
    scenario.targets.positions = scenario.targets.matrix;
end
```

Ambiguity Function Display

Plotting of the ambiguity functions.

```
function []= displayAmbiguityFunction(radarImage,data)
    switch radarImage.method
        case 'non-coherent'
            figure;
            sgtitle('Non-Coherent Processing');
            subplot(1,2,1)
            x=linspace(-10,10,128);
            plot(x,data(64,:)/max(data(64,:))) %Data transposed
            xlabel('X axis (m)')
            ylabel('A(X)');
            subplot(1,2,2)
            plot(x,data(:,64)/max(data(:,64))) %Sata transposed
            xlabel('Y axis (m)')
            ylabel('A(X)');
        case 'coherent'
            figure;
            sgtitle('Coherent Processing');
            x=linspace(-.1,.1,128);
            subplot(1,2,1)
            plot(x,data(64,:)/max(data(64,:)))
            xlabel('X axis (m)')
            ylabel('A(X)');
            subplot(1,2,2)
            plot(x,data(:,64)/max(data(:,64)))
            xlabel('Y axis (m)')
            ylabel('A(X)');
    end
end
```

Display Space Info

Plotting of the antennas and targets disposition.

```
function [] =displaySpaceInfo(scenario)

    figure('Position', [1000, 1000, 2*560, 1*420]);
    subplot(1,2,1);
    plot(scenario.tx.positions(:, 1), scenario.tx.positions(:, 2), 'r.', 'markerSize', 12);
    sgtitle('TX / RX Antennas & Target Distribution');
    axis([-10 10 -8 8]);
    hold on
    plot(scenario.rx.positions(:, 1), scenario.rx.positions(:, 2), 'c.', 'markerSize', 12);
    plot(scenario.targets.positions(:, 1), scenario.targets.positions(:, 2), 'k.',...
        'markerSize', 12);
    xlabel('(m)');
```

```
    ylabel('(m)');
    legend('Tx antennas','Rx antennas','Real Target position')
    hold off

    subplot(1,2,2);
    sgtitle('Target Distribution');
    axis([-.1 .1 -.1 .1]);
    hold on
    plot(scenario.targets.positions(:, 1), scenario.targets.positions(:, 2), 'k.',...
        'markerSize', 12);
    xlabel('(m)');
    ylabel('(m)');
    box on;
    legend('Real Target position')
    hold off
end
```